AWARD NUMBER: W81XWH-14-1-0502

TITLE: Smart Sensing and Dynamic Fitting for Enhanced Comfort and Performance of Prosthetics

PRINCIPAL INVESTIGATOR: Haiying Huang

CONTRACTING ORGANIZATION: University of Texas Arlington
                                Arlington, TX 76019

REPORT DATE: October 2017

TYPE OF REPORT: Annual

PREPARED FOR: U.S. Army Medical Research and Materiel Command
                Fort Detrick, Maryland 21702-5012

REPORT DOCUMENTATION PAGE

1. REPORT DATE	2. REPORT TYPE	3. DATES COVERED
October 2017	Annual	30 Sep 2016 - 29 Sep 2017

4. TITLE AND SUBTITLE
Smart Sensing and Dynamic Fitting for Enhanced Comfort and Performance of Prosthetics

5a. CONTRACT NUMBER

5b. GRANT NUMBER
W81XWH-14-1-0502

5c. PROGRAM ELEMENT NUMBER

6. AUTHOR(S)
Haiying Huang

E-Mail: huang@uta.edu

5d. PROJECT NUMBER

5e. TASK NUMBER

5f. WORK UNIT NUMBER

7. PERFORMING ORGANIZATION NAME(S) AND ADDRESS(ES)
University of Texas Arlington
JEREMY FORSBERG
400 S CORN ST
ARLINGTON, TX 76019-0001

8. PERFORMING ORGANIZATION REPORT NUMBER

9. SPONSORING / MONITORING AGENCY NAME(S) AND ADDRESS(ES)

U.S. Army Medical Research and Materiel Command
Fort Detrick, Maryland 21702-5012

10. SPONSOR/MONITOR'S ACRONYM(S)

11. SPONSOR/MONITOR'S REPORT NUMBER(S)

12. DISTRIBUTION / AVAILABILITY STATEMENT

Approved for Public Release; Distribution Unlimited

13. SUPPLEMENTARY NOTES

14. ABSTRACT

The objective of the project is to enhance the long-term fit and performance of prosthetic sockets through smart sensing, adaptive interface, and shear-based dynamic fitting strategy. In this project period (10/2016-9/2017), the sensor development effort has been focused on 1) implementing a test apparatus for calibration and testing of the antenna sensors in a condition imitating limb-socket interaction; 2) instrumenting a socket that can be worn by able-bodied volunteer to facilitate data collection and sensor calibration during walking; 3) establishing a procedure to design and calibrate the antenna shear and pressure sensor; 4) explore textile materials to produce robust antenna sensor that can be embedded in prosthetic liners; 5) investigating wireless interrogation of the antenna sensor without a connector; and 6) studying microstrip resonators for bio-impedance measurement. For actuation, we have 1) improved and de-bugged the prosthetic interface control hardware/software and tested the data acquisition system to improve the precision of the recorded and displayed pressure value within each gait cycle; 2) designed and built a working miniaturized control unit that reduced the weight by 63.5% (3.08 lb compared to the previous version of 4.85 lb) in weight and the volume by 56% (6''x6''x5'' compared to 10''x8''x4'' in the previous version).

15. SUBJECT TERMS
None listed

16. SECURITY CLASSIFICATION OF:			17. LIMITATION OF ABSTRACT	18. NUMBER OF PAGES	19a. NAME OF RESPONSIBLE PERSON USAMRMC
a. REPORT	**b. ABSTRACT**	**c. THIS PAGE**	Unclassified	40	**19b. TELEPHONE NUMBER** *(include area code)*
Unclassified	Unclassified	Unclassified			

Contents

1   INTRODUCTION

The objective of the project is to enhance the long-term fit and performance of prosthetic sockets through smart sensing, adaptive interface, and shear-based dynamic fitting strategy. In this project period (10/2016-9/2017), the sensor development effort has been focused on 1) implementing a test apparatus for calibration and testing of the antenna sensors in a condition imitating limb-socket interaction; 2) instrumenting a socket that can be worn by able-bodied volunteer to facilitate data collection and sensor calibration during walking; 3) establishing a procedure to design and calibrate the antenna shear and pressure sensor; 4) explore textile materials to produce robust antenna sensor that can be embedded in prosthetic liners; 5) investigating wireless interrogation of the antenna sensor without a connector; and 6) studying microstrip resonators for bio-impedance measurement. For actuation, we have 1) improved and de-bugged the prosthetic interface control hardware/software and tested the data acquisition system to improve the precision of the recorded and displayed pressure value within each gait cycle; 2) designed and built a working miniaturized control unit that reduced the weight by 63.5% (3.08 lb compared to the previous version of 4.85 lb) in weight and the volume by 56% (6''x6''x5'' compared to 10''x8''x4'' in the previous version).

2   KEYWORDS

Prosthetic socket, interface, shear/pressure sensor, antenna sensor, wireless interrogation, textile antenna sensor, bioimpedance, active interface, actuator inserts, PTB-AFO, Control System, Graphic User Interface (GUI), microprocessor

3   ACCOMPLISHMENTS

- **What were the major goals of the project?**

The three aims of the projects are: 1) Demonstrating real-time measurements of interfacial stresses and residual limb volume; 2) Producing active interfaces that can automatically adjust the fitting of the prosthetic socket; 3) Testing the active prosthetic interface and the shear-based fitting strategy in clinical settings.

First year milestones:
- *Milestone #1: Author manuscript that demonstrates simultaneous measurement of shear and pressure stresses (by July 2015) – journal paper accepted/published on line (*10.1109/JSEN.2017.2765893*)*
- *Milestone #2:Author manuscript that demonstrates volume and bio-impedance sensing using antenna sensors (postponed to 4th year)*
- *(Added) Demonstrate sensor implementation in custom made prosthetic liner - completed*
- *Milestone #4:Demonstrate a laboratory prototype that can dynamically change pressure profile (by September 2015) –completed*

Second year milestones:
- *Milestone #5: Demonstrate an active fitting system for subtask 5 (by October 2016) -75% completed*
- *Milestone #7: HRPO** approval received – completed*

3rd year milestones:
- *Milestone #3: Co-author manuscript that demonstrates real-time interrogation of sensor inserts – experiment completed*
- *Milestone #6: Co-author manuscript that demonstrates real-time adaptive fitting and shear-based fitting in laboratory settings – post-ponded to 4th year*
- *Milestone #8: Co-author manuscript and final report on clinical test results - postponed to 4th year*

- **What was accomplished under these goals?**

Accomplishment #1: Developed test apparatus for calibrating the smart liner in conditions imitating socket-limb interaction
- **Specific objective:** establish a method to calibrate the embedded sensor in a controlled and repeatable environment
- **Major activities**:
1) Developed a test apparatus that imitates the condition of a socket: a test apparatus was developed to ensure repeatable tests of the fabricated smart liner. The design of the test apparatus is shown in Figure 1(a). At the design phase, the residual limb is imitated using a conical cylinder that is situated at the center of two semi-circle rings. Three cantilever beam load-cells (CBLcs) were mounted on the semi-circle rings to apply pressures to the residual limb as well as to measure the shear and pressure loads using the strain gauges. The CBLCs are installed on linear translation stages and articulating arms with ball-pivot assemblies so that they can be positioned at different heights, pressures, and angles independently. A linear motor was implemented at the base of the test apparatus and connected to the conic cylinder through a commercial load cell. As such, both static and dynamic tests can be carried out. In addition, an LVDT distance sensor was installed to measure the vertical displacement of the conical cylinder. The test fixture can be configured for testing on a synthetic limb or on the leg of a volunteer, as shown in Figures 1(b) and 1(c).
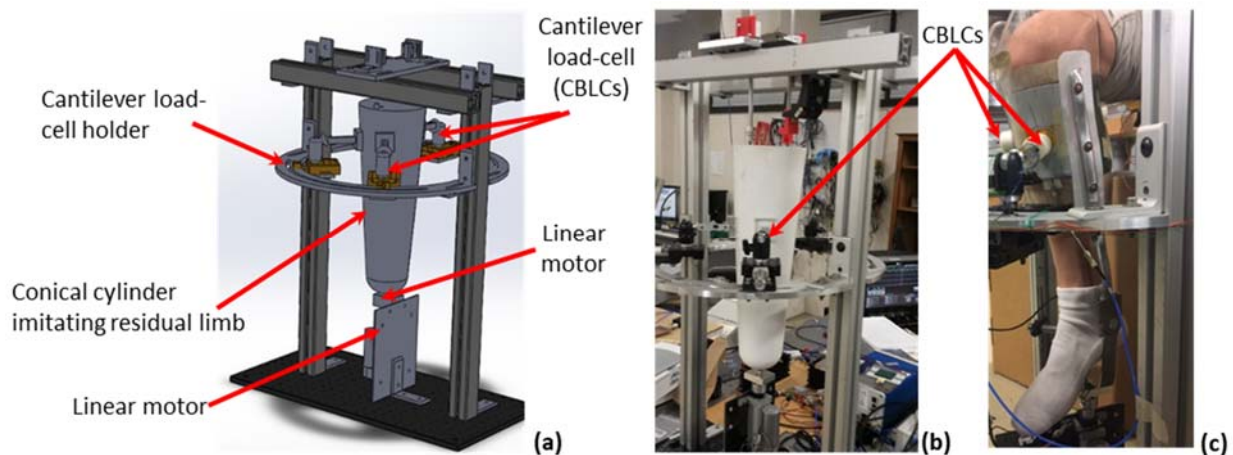

Figure 1: test apparatus for characterizing the antenna sensor in a simulated limb-socket condition; (a) design model; (b) hardware implementation using a cylindrical cone as the synthetic limb; (c) testing of the prosthetic liner worn by a volunteer.

Implement Arduino-based controllers for motor control and sensor data acquisition: the test apparatus is controlled by two Arduino based microprocessors; an Arduino Uno is implemented to control the motor so that the movement of the synthetic leg can be controlled independently from the data acquisition. An Arduino Mega 2560 equipped with a custom built shield was implemented to collect sensor data. The board layout of the Arduino Mega shield is shown in Figure 2(a). Six Wheatstone bridges were implemented for converting the resistance changes of the strain gauges to small voltage signals. The Wheatstone bridge outputs are amplified and acquired as analog signals by the Arduino Mega. An amplifier circuit was also implemented on the shield to amplify the commercial load-cell output. Finally, a 5V voltage is supplied to the LVDT sensor and its analog output is acquired using the Arduino Mega. The controllers communicate to a PC through the serial port. The Arduino software accepts a variety of commands via a custom command parser embedded into the microcontroller.
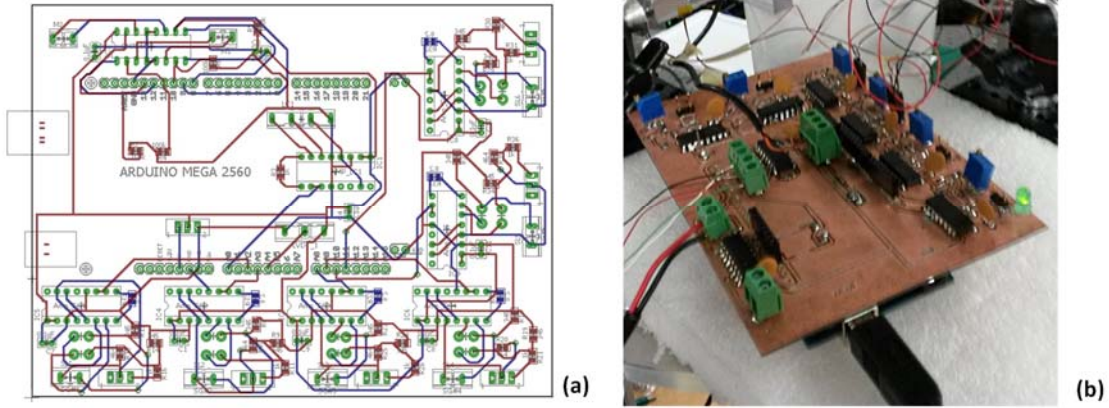
3

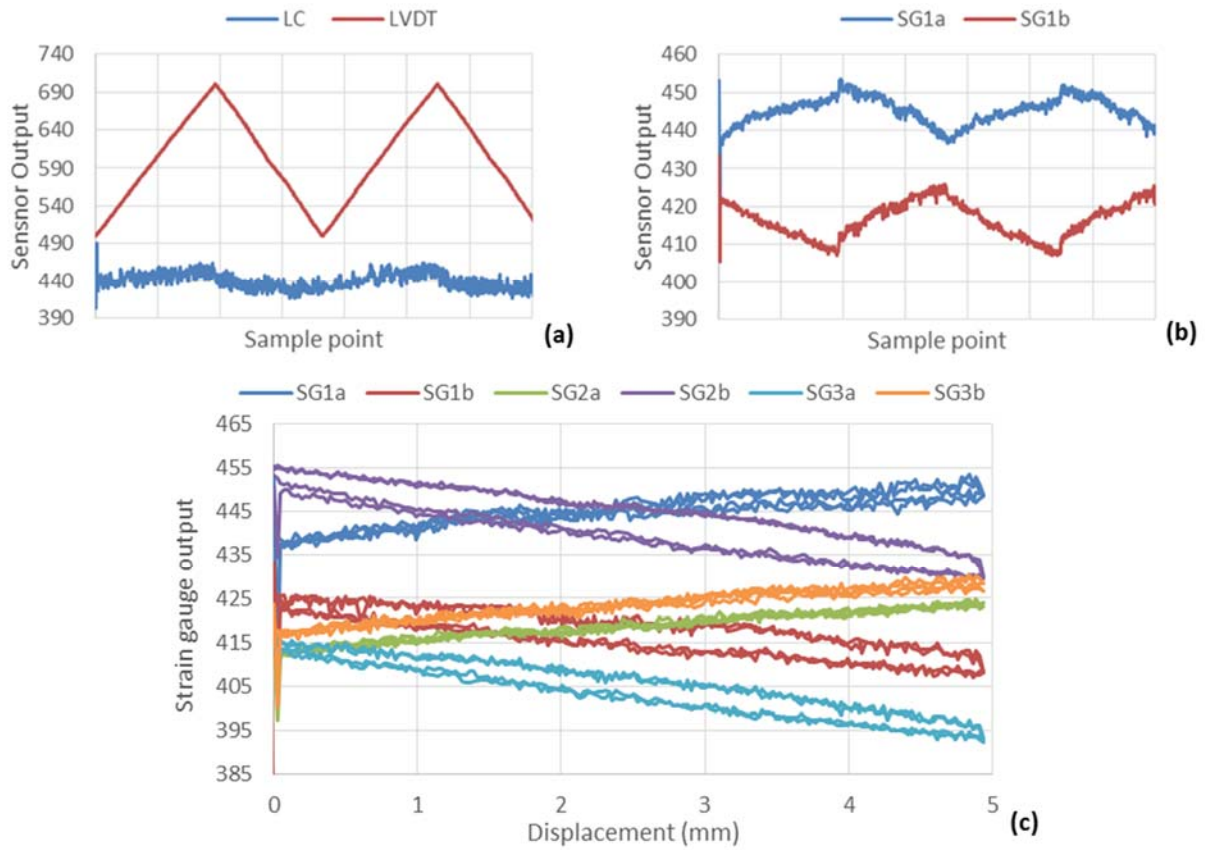Figure 2: Arduino shield for sensor signal conditioning; (a) board layout; (b) hardware implementation.

Figure 3: sensor data collected while the synthetic limb was moved up and down 4.96 mm for two cycles; (a) load cell and LVDT distance sensor outputs; (b): strain gauge outputs of CBLC #1. (c) strain gauge outputs vs. the displacement measured by the LVDT showing repeatability and linearity of the measurements.

- **Significant results:** the sensor data acquired continuously from the load cell (LC), LVDT, and the three CBLCs are shown in Figure 3 when the motor moved the synthetic limb up and down in two cycles. The total distance moved, measured by the LVDT sensors, was 4.96 mm. As shown in Figure 3(a), the load cell reading changed very little. Since the synthetic limb was supported by the three CBLCs only and the liner was soft, very little force was needed to move the synthetic limb. The load cell essentially measures the weight of the synthetic limb. The strain gauge output of the CBLC #1, shown in Figure 3(b), varied linearly with the displacement of the synthetic limb. The other two CBLCs produced results

4

similar to those shown in Figure 3(b). Plotting the strain gauge outputs versus the displacement measured by the LVDT indicated that the strain gauges produced repeatable results for the two cycles of movement. In addition, it was observed that the strain gauges that are under tension when the synthetic limb was moving up did not show any hysteresis while the strain gauges that are under compression when the synthetic limb was moving up displayed small degree of hysteresis, as shown in Figure 3(c).

Accomplishment #2: Instrumented a socket that can be worn by an able-bodied volunteer for sensor calibration
- **Specific objective:** achieve in-socket sensor calibration and un-tethered data acquisition during walking
- **Major activities**:
1) <u>Fabricate and instrument a prosthetic socket for testing on an able-bodied volunteer</u>: with the help of the clinicians at UT Southwestern, a socket was custom made for the volunteer. As shown in Figure 4(a), the custom-made socket was made in one piece with an open bottom so that the volunteer can slide her foot through the opening. A steel braces was mounted on the socket for the volunteer to walk while wearing the socket. To test the socket in the test apparatus shown in achievement #1, a screw hole was tapped at the bottom of the steel braces so that it can be attached to the load cell and the linear motor, as shown in Figure 1(c). Three openings were cut at the load bearing areas (i.e. at the medial tibia, the lateral tibia, and the popliteal depression) and on CBLC was mounted on the socket. The socket worn by a volunteer in shown in Figure 4(b).
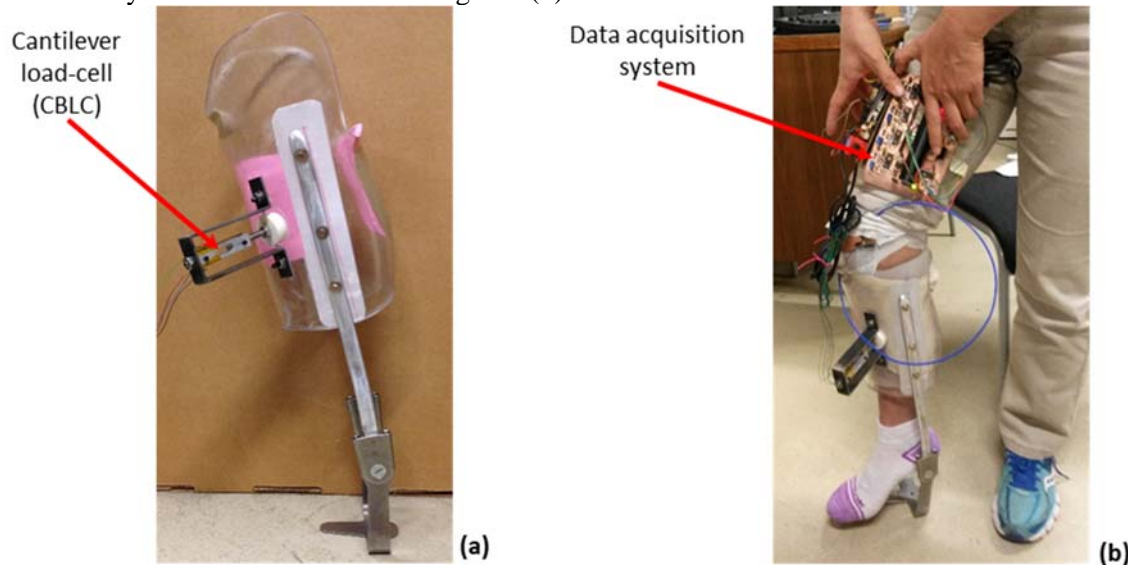

Figure 4: (a) a prosthetic socket instrumented with a cantilever beam load cell for antenna sensor calibration; (b) the socket worn by an able-bodied volunteer with untethered data acquisition systems.

2) <u>Implemented a portable wireless data acquisitions system to acquire data dynamically from the socket</u>: an ARM processor based data acquisition system was developed to acquire the sensor data from the antenna sensor dynamically while the Arduino-based controlled described in achieve #1 can be used to collect the strain gauge outputs from the CBLCs. To achieve a complete untethered operation of the instrumented socket, both controllers are equipped with Bluetooth radio modules so that the data can be transmitted wirelessly while the volunteer is walking. The data acquisition systems can be attached to the wearer's leg and are completely un-tethered, as shown in Figure 4(b). An android-based application software was developed to receive the data wirelessly and display them on an android device.

- **Significant results:** the sensor data collected from the CBLC strain gauges and the antenna sensors, while the volunteer lifted and lowered the socket are shown in Figure 5. As shown in Figure 5(a), the strain gauge outputs responded well when the socket was lifted and lowered. The two strain gauge outputs have opposite trends, indicated that the CBLC was subjected to bending due to the shear force applied at its end. Since the strain gauge outputs and the antenna sensor outputs were received using two separate android devices, the antenna sensor output shown in Figure 5(b) cannot be correlated to the strain gauge data shown in Figure 5(a). Clearly the antenna sensor is responding to the movement of the socket. In the coming quarter, the two data acquisition systems will be synchronized so that these two sets of data can be correlated and the antenna sensor outputs can be calibrated by the strain gauge outputs.
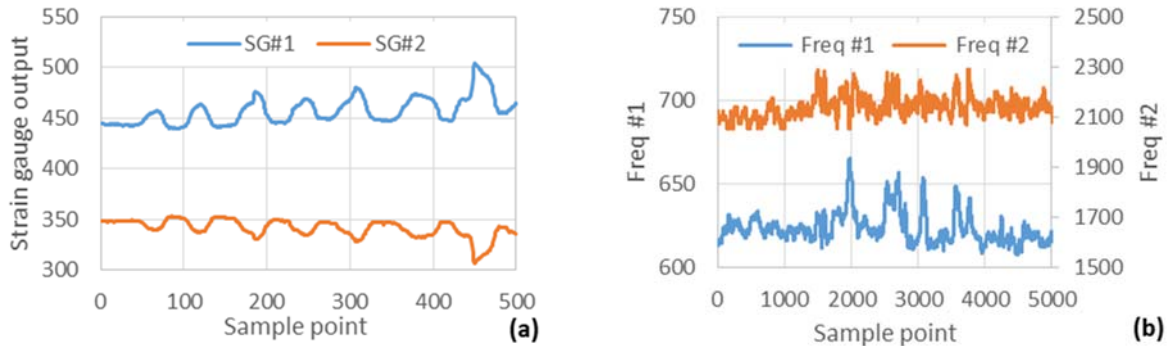

Figure 5: sensor data received wirelessly while the volunteer was lifting and lowering the socket; (a) CBLC strain gauge outputs; (b) antenna sensor outputs.

Accomplishment #3: Established a systematic approach to evaluate the antenna sensor for shear and pressure sensing
- **Specific objective:** 1) validate the principle of operation of using antenna sensor for shear and pressure sensing; 2) publish the research results as peer-reviewed journal paper
- **Major activities**:
1) <u>Simulate the effects of superstrate on the antenna resonant frequencies</u>: to evaluate the effects of the superstrate on the antenna resonant frequencies, a single-frequency patch antenna with a resonant frequency of 6 GHz was modeled using an EM simulation tool (Sonnet Pro 16.52). The simulated antenna resonant frequency is plotted verses the superstrate dielectric constant in Figure 6. It was found that the antenna resonant frequency reduced linearly with the increase of the superstrate dielectric constant. Based on the resonant frequency shifts, we can determine the effective dielectric constant of the antenna, which linearly increases with the superstrate dielectric constant, as shown in Figure 6. This approach can be used in the future to experimentally determine the dielectric constant of the superstrate and incorporate the measured dielectric constant in the antenna sensor design process. As such, a more realistic antenna design model can be established for sensor optimization and parametric study.
2) <u>Characterize the sensitivity of the antenna sensor with different configurations</u>: the sensitivities of the antenna shear and pressure sensor with different configurations were characterized with and without of the superstrate material using a motorized three-axis translation stage as well as the bench-top shear and pressure test fixture. Directors of two different shapes, i.e. U-shape and a rectangular shape, were evaluated. In addition, different orientations of the director relative to the microstrip transmission line were also evaluated.
3) <u>Redesign the antenna sensor to achieve higher gains and smaller size:</u> based on the comparative studies on the sensitivities of different antenna sensor configurations and director shapes, we discovered that
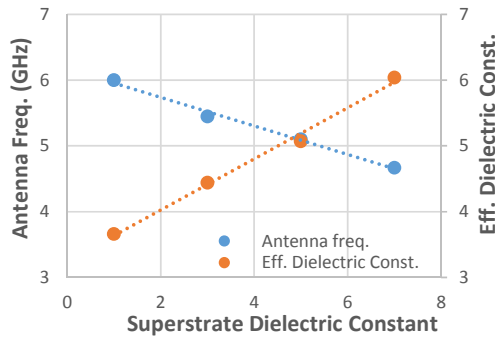
6

Figure 6: effect of superstrate dielectric constant on the antenna resonant frequency and the effective dielectric constant derived from the antenna resonant frequency shift.
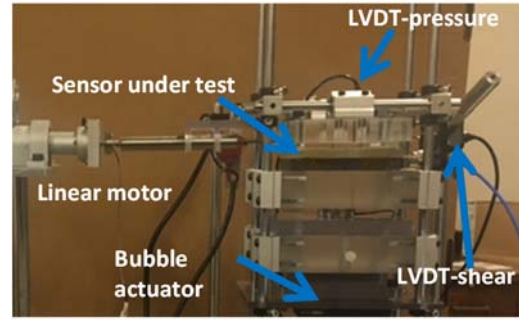

Figure 7: mechanical test fixture for applying controlled shear and pressure displacements on the antenna sensor under test.

the antenna sensitivity is strongly influenced by the gain of the rectangular patch antenna. Therefore, the rectangular antenna was redesigned to achieve maximum gain and optimized impedance matching. The sensor size was chosen to be around 10 mm. The f_{01} and f_{10} frequencies were selected to be 5.5 and 6.5 GHz, respectively, which resulted in a radiation patch that is 10.4 mm in length and 12.4 mm in width. For the design of the microstrip transmission line, a typical transmission line width of 1.0 mm was chosen, which has an impedance of 86.3 Ω for an effective dielectric constant of 4.45. The inset feeding location (x_0, y_0) was calculated accordingly. Finally, a quarter-wavelength (Q-λ) transformer was designed to match the impedances of the radiation patch and the SMA connector. The impedance of the Q-λ transformer was calculated as $Z_q = \sqrt{Z_{50} \times Z_t} = 65.7$ Ω, where Z_{50} represents the 50 Ω impedance of the SMA connector and $Z_t = 86.3$ Ω is the impedance of microstrip transmission line. The corresponding width and length of the Q-λ transformer are 1.71 mm and 6.4 mm, respectively. The dimensions of the director were chosen to be 12 mm in length and 16 mm in width. The sensor design was modelled in Sonnet Pro. Due to the inset feeding, the impedances of the two antenna modes are coupled. To find an optimized feeding location, a parameter sweep on (x_0, y_0) was carried out. In addition, the width direction of the radiation patch was reduced to compensate for the additional electric length of the TM$_{10}$ mode due to the inset feeding.

4) Validate the high sensitivity of the improved antenna design: the improved antenna design was fabricated and tested using the bench-top shear and pressure test fixture. As shown in Figure 7, the sensor package is sandwiched between two plates; the top plate is fixed along the vertical direction but can freely slide along the horizontal direction. The bottom plate is mounted above a bubble actuator and can freely slide along the vertical direction. Inflating the bubble actuator pushes the bottom plate upward, generating a pressure force on the sensor package. The displacement of the bottom plate is measured using a linear variable differential transformer (LVDT) distance sensor. To apply the shear displacement, a rod was screwed on the top plate and its position can be automatically adjusted using a linear motor. The shear displacement of the top plate was again measured using an LVDT distance sensor, mounted on the opposite side of the shear rod. The resonant frequencies of the microstrip patch antenna were measured by connecting the microstrip patch antenna to a vector network analyzer (VNA) (Rohde & Schwarz, ZVA24) using a coaxial cable. The frequency range of the VNA was set to be swept from 4.5 GHz to 7.5 GHz with 5001 frequency points, resulting in a frequency resolution of 0.6 MHz. The S11 curve of the antenna sensor was measured under different combinations of shear and pressure displacements. An Arduino-based controller was implemented to control the applied shear and pressure displacements and to acquire the shear and pressure displacements from the LVDT sensors. A visual-basic program was developed in Microsoft Excel to communicate with the controller and to acquire the S11 parameters from the VNA automatically.

- **Significant results:**
1) <u>Validated the simulated effect of the superstrate with experiment measurements</u>: the simulated and measured resonant frequencies of the antenna without the superstrate, with the superstrate, and with the superstrate and the director are shown in Figure 8. For both cases, the director was placed to cover half of the radiation patch along its length direction and was centered along the width direction of the radiation patch. As expected, the antenna frequencies shift to lower frequencies when the superstrate was placed on top of the radiation patch. In addition to the frequency shifts, the bandwidths of both resonances also increased. Adding the director, however, shifted the antenna frequencies closer to their original positions. The measured resonant frequency shifts due to the superstrate are much smaller than the simulated values, indicating that the dielectric constant of the superstrate material is smaller than the assumed value of 3.0. Nonetheless, the fabricated antenna sensor displayed acceptable return losses and bandwidths for both resonances.
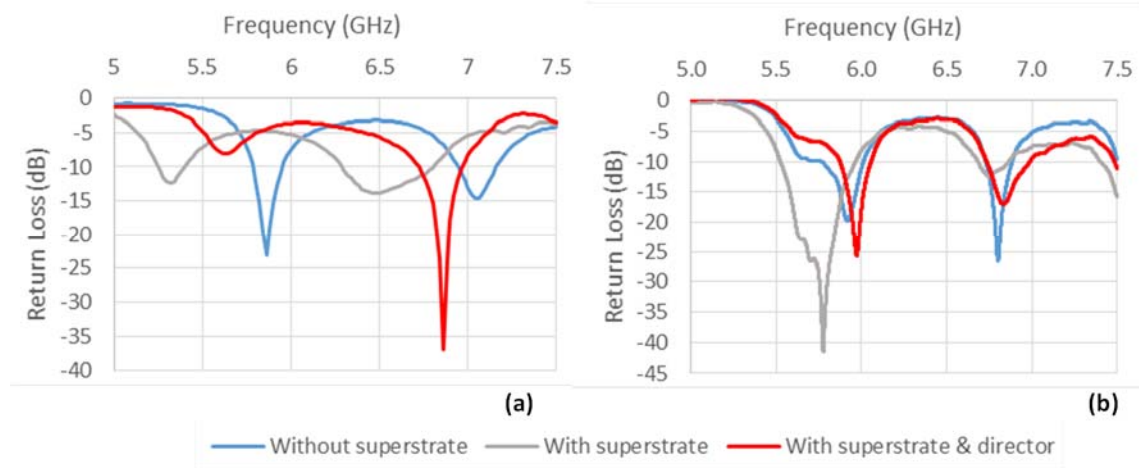

Figure 8: simulated and measured antenna resonant frequencies without the superstrate, with the superstrate, and with the superstrate and director; (a) simulation results; (b) measurement results.
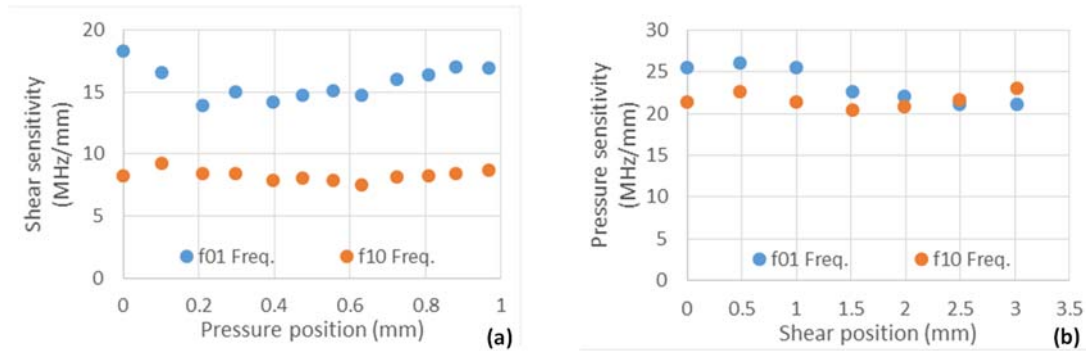
Figure 9: pressure and shear sensitivities of the improved antenna sensor; (a) shear sensitivity at different pressure positions; (b) pressure sensitivity at different shear positions.

2) <u>Achieved an order of magnitude improvement on the antenna gain with the new antenna design</u>: the shear and pressure sensitivities of the antenna resonant frequencies are shown in Figure 9. The shear sensitivity of the f_{01} frequency is around 15 MHz/mm while the shear sensitivity of the f_{10} frequency is about 8 MHz/mm. The improvement on the antenna sensor is about one order of magnitude higher than the previous antenna design. The pressure position does not appear to have a large effect on the shear sensitivities, especially for the f_{10} frequency. The pressure sensitivities of these two antenna resonant

8

frequencies are similar, as shown in Figure 9(b). The variations of the pressure sensitivities to the shear position were found to be small as well.

Accomplishment #4: explore textile material as substrate to improve sensor robustness
- **Specific objective:** produce sensors that can sustain repeated rolling during donning on and off
- **Major activities**:
1) Evaluate the robustness of the microstrip transmission line fabricated from different textile materials: while embedding the antenna sensor fabricated on flexible substrates RO3003 into the silicone liner, we discovered that the RO3003 substrate, while being flexible, cannot sustain the rolling motion during donning on and off. The copper trace frequently delaminated from the substrate, buckled, and broke in a few cycles of bending. To improve the sensor robustness, common textile materials were investigated to serve as the dielectric substrate and for improving the adhesion of the silicone material to the conductive materials of copper or Pyralus. Three different textile materials, i.e. 0.5 mm and 1 mm thick Denim, canvas, and felt, were studied as the substrate material. Canvas, thin cotton, and polyester cloth were laminated on the transmission line as well as the ground plane to improve the adhesion to silicone. The transmission lines were constructed layer by layer using an iron-on adhesive film as the bonding agency. The final assemblies of the transmission line embedded in silicone are shown in Figure 10. To evaluate the robustness of the fabricated transmission lines, the transmission lines were rolled using a 22 mm diameter roller and the connectivity of the transmission line was tested after performing 10 rolls each time.
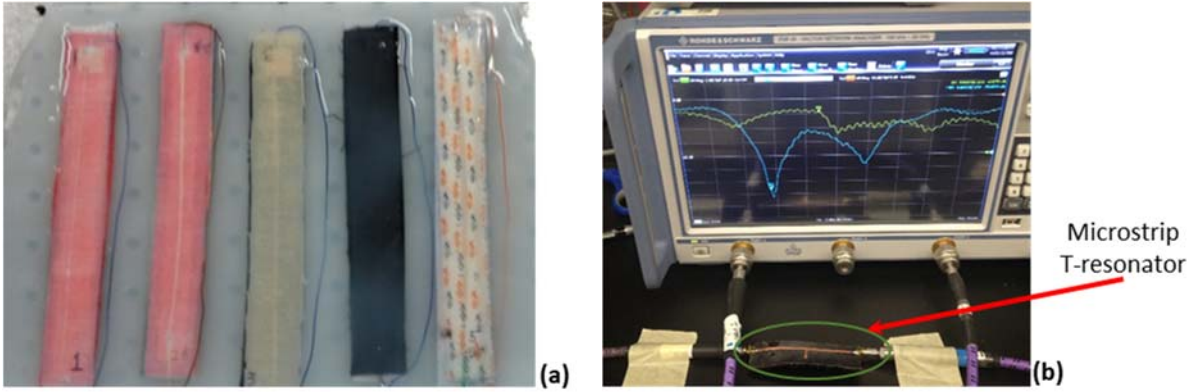

Figure 10: (a) microstrip transmission lines fabricated from different textile materials and embedded in silicone; (b) experiment setup for characterizing the microstrip T-resonator fabricated on denim.

2) Measure the dielectric constant of denim material: in order to use the denim material as the substrate, the dielectric constant of the denim has to be measured first. A microstrip T-resonator was employed for this purpose, which can also later to be used for the bio-impedance measurement. A T-resonator, as shown in Figure 10(b), has a very simple configuration of a open stub connected to the microstrip transmission line at a 90 degree angle. The open stub functions as a resonator that resonates at odd integer multipliers of its quarter-wavelength frequencies. In other words, if the stub has a length of d, the fundamental resonant frequency of the T-resonator is $f = \frac{c}{4d\sqrt{\varepsilon_{reff}}}$. When the medium above the T-resonator is air, the effective dielectric constant can be calculated as $\varepsilon_{reff} = \frac{\varepsilon_r+1}{2} + \frac{\varepsilon_r-1}{2\sqrt{1+10h/w}}$, in which ε_r is the dielectric constant of the substrate, h is the height of the substrate, and w is the width of the transmission line. Therefore, the dielectric constant of the substrate ε_r can be measured from the resonant frequency of the T-resonator as long as the length of the open stub is known. When the T-resonator is placed next to the human body, the dielectric constant of the human tissue also contributes to the effective dielectric constant ε_{reff}. As such, the changes in the dielectric constant of the tissue can be detected from the resonant frequency shift of the T-resonator. The T-resonator shown in Figure 10(b)

was designed based on a dielectric constant of 1.7 for the denim, as reported in the literature. The designed pattern was cut from copper tapes using a computer-aided pattern-cutting machine and laminated on the denim using iron-on adhesive.

3) <u>Explore rapid-prototyping fabrication technique:</u> to fabricate the antenna sensor using textile materials, we investigated rapid-prototyping fabrication techniques using computer-aided pattern-cutting machines to cut the antenna pattern out of copper films. It takes the machine a few minutes to cut the pattern, as compared to a few hours using the chemical etching technique. The cut antenna pattern is transferred to the adhesive film for laminating on the textile material. In addition to being fast, the rapid-prototyping fabrication technique is also economical and has a large cutting area, which could be beneficial later in the project to produce large-size antenna arrays.

- **Significant results:**

1) <u>Validated the dielectric constant of the denim material:</u> the S21 parameters of two T-resonator, fabricated using copper film and 0.5 mm thick Denim, are compared with the simulation results in Figure 11(a). The two T-resonators have slightly different resonator frequencies, either due to the variation in the dielectric constant of the denim or the fabrication uncertainty. The dielectric constants calculated from the measured resonant frequencies are 1.79 and 1.91, respectively, which is close to the value of 1.7 reported in the literature. The average of the two measured dielectric constants was adopted for the antenna sensor design using denim as the substrate material. To evaluate the sensitivity of the T-resonator to the dielectric constant change of the superstrate, another layer of denim was laminated on top of the T-resonator and the measured S21 parameter of the T-resonator with the superstrate is shown in Figure 11(b). As expected, the superstrate shifted the resonate frequency of the T-resonator to a lower value. The measured effective dielectric constants of the substrate was 1.8 and 1.92, which are very close to the simulated values of 1.74 and 1.84.
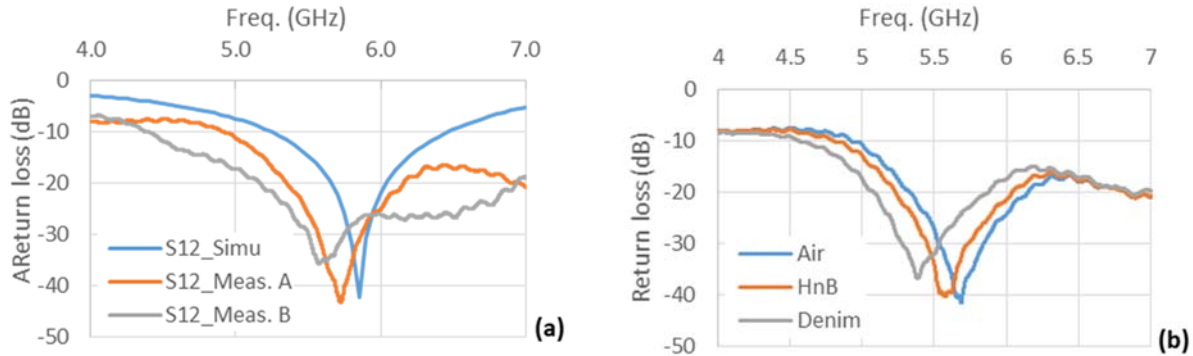

Figure 11: (a) comparison between the measured and simulated S_{21} parameters of two microstrip T-resonators fabricated on denim; (b) the effect of the superstrate (i.e. iron-on adhesive HnB and Denim) on the S21 parameter of the T-resonator.

2) <u>Characterized antenna sensor fabricated on denim</u>: antenna sensors with different length of transmission line were fabricated using 0.5 mm thick denim. Figure 12(a) shows the photos of the antenna sensor with 150 mm and 200 mm long transmission lines. The blue curve in Figure 12(b) shows the S11 parameter of an antenna sensor with a 200 mm long transmission line measured directly using a VNA. Due to the reflection at the SMA connector, the as-measured S11 parameter contains interference fringes that make determining the antenna resonant frequency difficult. Processing the S11 parameters using a post-processing algorithm can remove these fringes and produced a clean spectrum that clearly shows the antenna sensor resonates at 5.3 GHz and 6.2 GHz (see the red curve in Figure 12(b)). The antenna sensor with a 150 mm long transmission line shows less fringes and was used in the experiment shown in Figure 4(b) to obtain the data shown in Figure 5(b). Further characterization of the antenna sensor fabricated on denim substrates will be carried out following the procedure described in achievement #3.
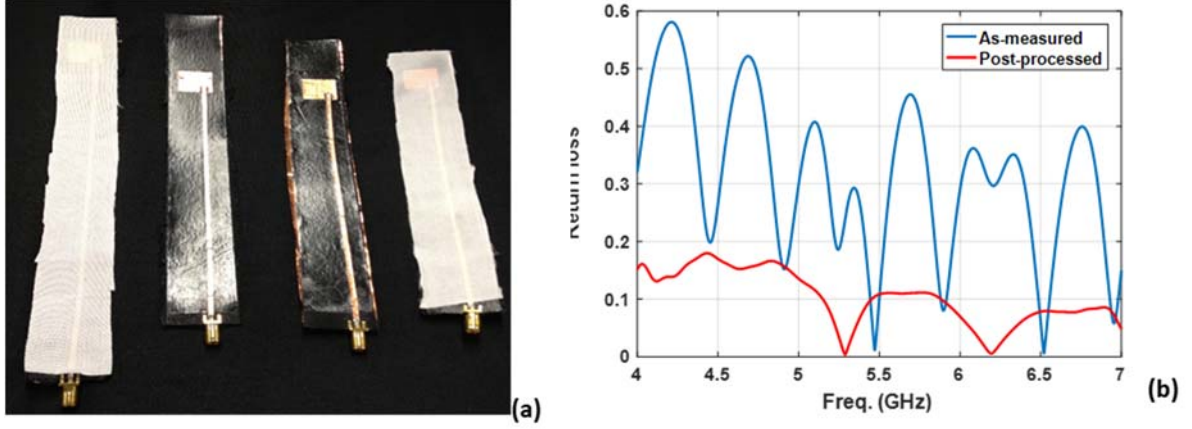
Figure 12: (a) a photo of antenna sensors fabricated on denim with150 mm and 200 mm transmission lines; (b) the S11 parameter of an antenna sensor with a 200 mm long transmission line measured directly using a VNA and the post-processed S11 parameter showing the two resonant frequencies.
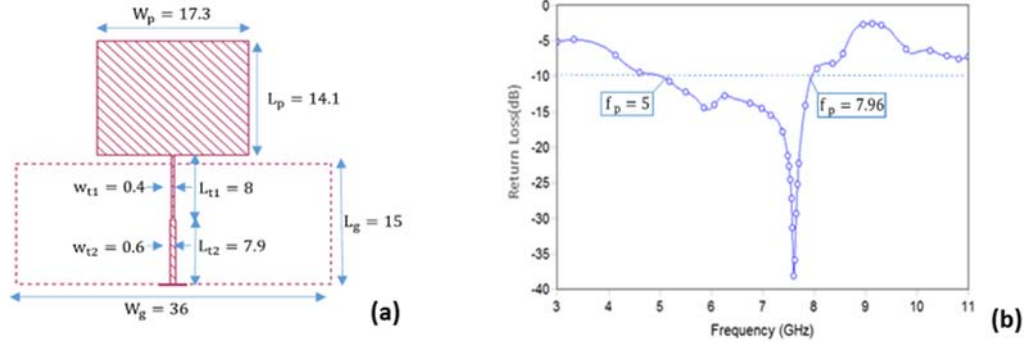

Figure 13: design of the UWB Tx/Rx antenna; (a) numerical simulation model; (b) simulated S11 parameter of the UWB Tx/Rx antenna. The -10 dB bandwidth is determined to be from 5 GHz to 7.96 GHz.

Accomplishment #5: Demonstrate wireless interrogation of the antenna sensor without connector
- **Specific objective:** improve the robustness of the embedded sensor by removing the connector
- **Major activities**:
1) <u>Design and characterize UWB Tx/Rx antenna fabricated on flexible substrates</u>: one of the challenges in implementing the antenna sensor on flexible substrates is the connector. The transmission line frequently breaks at the interface between the transmission line and the connector pin. In addition, the connector also creates a large reflection that generates interference fringes when the antenna sensor has a long transmission line (see the blue curve in Figure 12(b)). It is therefore desirable to interrogate the antenna sensor without a connector. By connecting an UWB Tx/Rx antenna to the antenna sensor, signals can be transmitted to and from the antenna sensor via the UWB antenna. The design of the UWB Tx/Rx antenna started with a conventional patch antenna having a perfect ground plane. To increase the bandwidth of the antenna, the ground plane has to be reduced to partially cover the radiation patch, as shown in Figure 13(a). Simulations of the antenna with perfect ground and partial ground were carried out, followed by the parametric study on the height of the ground patch and width of the microstrip feed line. Parametric studies was also carried out to evaluate the effect of the substrate thickness on the antenna bandwidth. It was discovered that the substrate thickness does not have a large effect on the antenna bandwidth as long as it is larger than 0.25 mm. The S11 parameters of the optimized UWB antenna is shown in Figure 13(b).
2) <u>Design the sensor package</u>: the antenna sensor and UWB antenna were designed to be fabricated on commercial substrate RO3003. The sensor size was chosen to be around 13 mm. The f_{01} and f_{10}

11

frequencies were selected to be 5.3 and 6.05 GHz, respectively, which resulted in a radiation patch that is 13.5 mm in length and 14 mm in width. For the design of the microstrip transmission line, a typical transmission line width and length of 0.62 mm and 210 mm was chosen. The sensor design was modelled in Sonnet Pro. Due to the inset feeding, the impedances of the two antenna modes are coupled. To find an optimized feeding location, a parameter sweep on (x0, y0) was carried out.

3) <u>Implement the wireless interrogation scheme:</u> the experimental set up for wireless interrogation of the antenna sensor without connector is shown in Figure 14. The sensor node was placed in the prosthetic socket covered by liner. The wireless interrogator was realized by using two circular UWB Tx/Rx antenna. The UWB Tx/Rx antenna were placed at an interrogation distance of 5 cm in front of Tx/Rx antenna of the sensor node. The S21 parameter of the two interrogator UWB antenna was measured using a VNA and the antenna backscattering was extracted using a post-processing algorithm. For more details of the wireless interrogation scheme, please refer to the published journal paper (Yao, J., Tchafa, F. E., Jain, A., Tjuatja, S. and **Huang, H.**, 2016, "Far-field Interrogation of Microstrip Patch Antenna for Temperature Sensing without Electronics", *IEEE Sensors Journal,* v16, n19, p 7053 - 7060.).
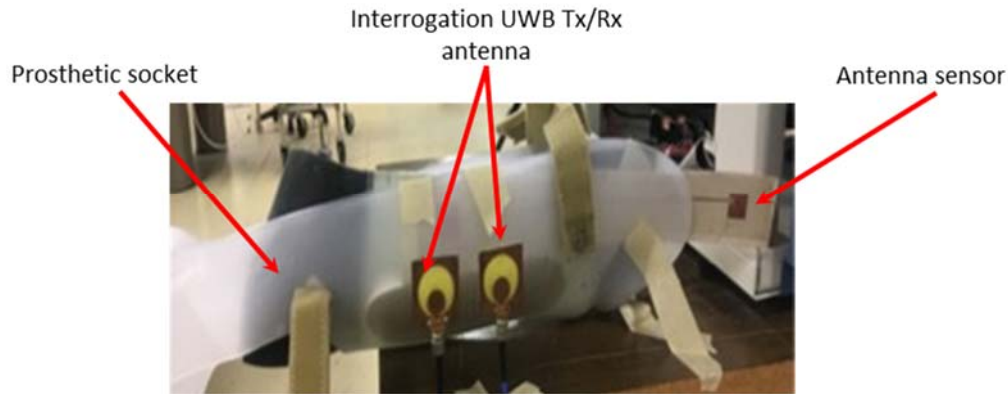
Figure 14: wireless interrogation of the antenna sensor placed inside of a socket.

- **Significant results:**
1) <u>Validated that the UWB Tx/Rx microstrip antenna fabricated on 0.25 mm flexible substrate has sufficient bandwidth:</u> The UWB Tx/Rx microstrip antenna was fabricated on the selected substrate using chemical etching and the front and back views of the fabricated antenna are shown in Figure 15(a). The measured S11 curve is plotted in Figure 15(b), which validated that the fabricated UWB Tx/Rx antenna has the operating bandwidth from 3.4 GHz to 8.6 GHz.

Figure 15: UWB Tx/Rx microstrip antenna fabricated on flexible substrate and its S11 parameter measured by a Vector Network Analyzer (VNA); (a) front and back views of the fabricated UWB Tx/Rx microstrip antenna; (b) the measured S11 curve. The -10 dB bandwidth of the UWB Tx/Rx antenna is from 3.4 GHz to 8.6 GHz.

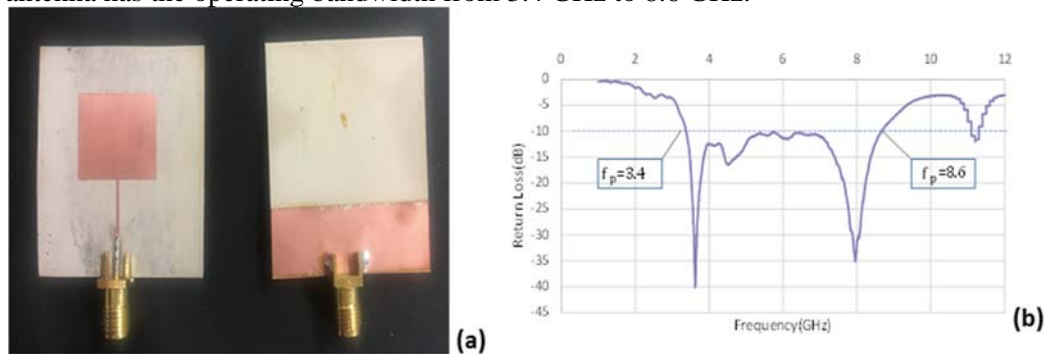2) <u>Demonstrate wireless interrogation of the antenna sensor without any connectors:</u> the entire sensor node was fabricated on the flexible substrate using chemical etching and the picture of its front is shown in Figure 16(a). The transmission line connecting the Tx/Rx UWB antenna and the sensor antenna is 200 mm long. The time domain signal calculated from the measured S21 parameter is shown in Figure 16(b). Finally, the antenna mode backscattering was extracted by time gating the time domain signal from 1.8 ns to 3 ns. The resonant frequency of the antenna sensor can then be determined by performing FFT of the time-gated signal. As shown in Figure 16(c), the spectrum of the time gated signal shows two valleys; one at 4.95 GHz and the other at 6.08 GHz, which match well when the resonant frequencies of the antenna sensor when it is measured using a connector.
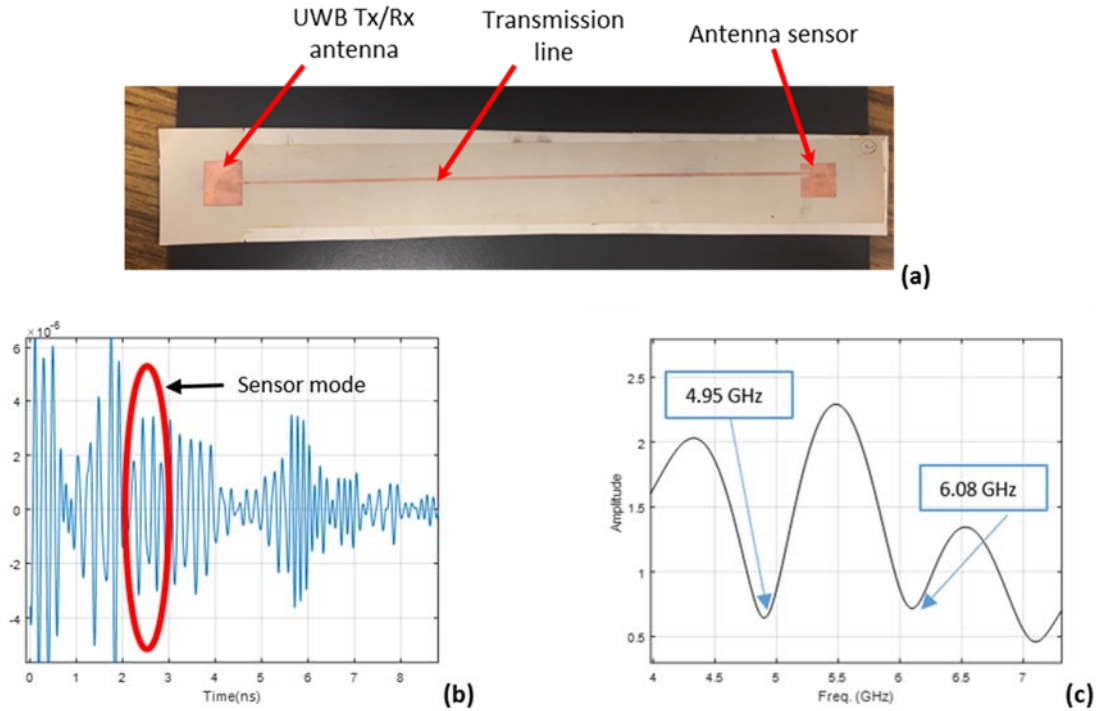

Figure 16: wireless interrogation of the antenna sensor without a connector; (a) experiment set up; (b) time-domain signal calculated from the measured S21 parameter. (c) spectrum of the antenna backscattering time-gated from the signal shown in (b) shows two valleys that correspond to the antenna resonance.

Accomplishment #6: investigate microwave resonator for bio-impedance measurement

- **Specific objective:** evaluate microstrip Fabry-Perot resonator for bio-impedance sensing
- **Major activities**: a Fabry-Perot cavity is generated in a microstrip transmission line when the transmission line has two reflection points separated by a distance d. Due to the interference of these two reflected waves, the spectrum of the reflected signal display fringe patterns whose spectral spacing is depended of the effective cavity distance, which can be calculated as $d_{eff} = \sqrt{\varepsilon_{reff}}\,d$, in which d is the physical length between the two reflection points and ε_{reff} is the effective dielectric constant. By placing the Fabry-Perot cavity next to the human body, the human tissue becomes the superstrate of the transmission line and thus changes ε_{reff}. Analyzing the reflectance spectrum of the Fabry-Perot cavity, therefore, can determine the dielectric constant of the human tissue. To validate this hypothesis, a transmission line of 152.4 mm (6 inch) in length and 1 mm in width was designed on a RO4350 substrate with dielectric constant of 3.48 and simulated using an EM simulation tool, HFSS. Since the impedance of the transmission line has an impedance of 67.8 Ω, reflections are generated at the input port and at the end of the transmission line. As such, the entire transmission line functions as a Fabry-Perot cavity. In addition, a slit of 0.2 mm in length and 0.5 mm in width was created at a distance of 101.5 mm from the input port. The presence of slit creates three cavities: i) between the port and the

13

slit with a cavity distance of 101.5 mm. ii) between the slit and the end with a cavity distance of 50.7 mm; iii) between the input port to the end with a cavity distance of 152.4 mm. To extract the cavity distances from the reflectance spectrum of the Fabry-Perot cavities, A MATLAB program was developed to 1) to time gate the signals for a specific cavity; and 2) to calculate the cavity distance based on the spectrum of the time-gated signal. For the first purpose, the as-acquired reflectance spectrum of the microstrip transmission line, which may contain multiple cavity, is converted to the time domain using the Inverse Fast Fourier Transform (IFFT). Time-gating is then applied based on the estimated time span of a specific cavity. Next, the spectrum of the time-gated signal was converted back to the spectrum domain using Fast Fourier Transform (FFT). The cavity distance d can then be determined from the fringe spacing f_p as $d = \frac{f_p}{2\sqrt{\varepsilon_{reff}}}$, assuming ε_{reff} is known. Similarly, if the cavity distance d is know, then ε_{reff} can be determined as $\varepsilon_{reff} = \left(\frac{f_p}{2d}\right)^2$. The MATLAB algorithm was validated using both simulated and measured fringe spectra.

- **Significant results:** Figure 17(a) shows the time-domain signal converted from the simulated and measured S11 parameters of the transmission line without a slit. The reflection at time zero is due to the impedance mismatch between the SMA connector and the transmission line. The large signal at around 1.9 ns is generated at the end of the transmission line. In comparison, the reflection signal
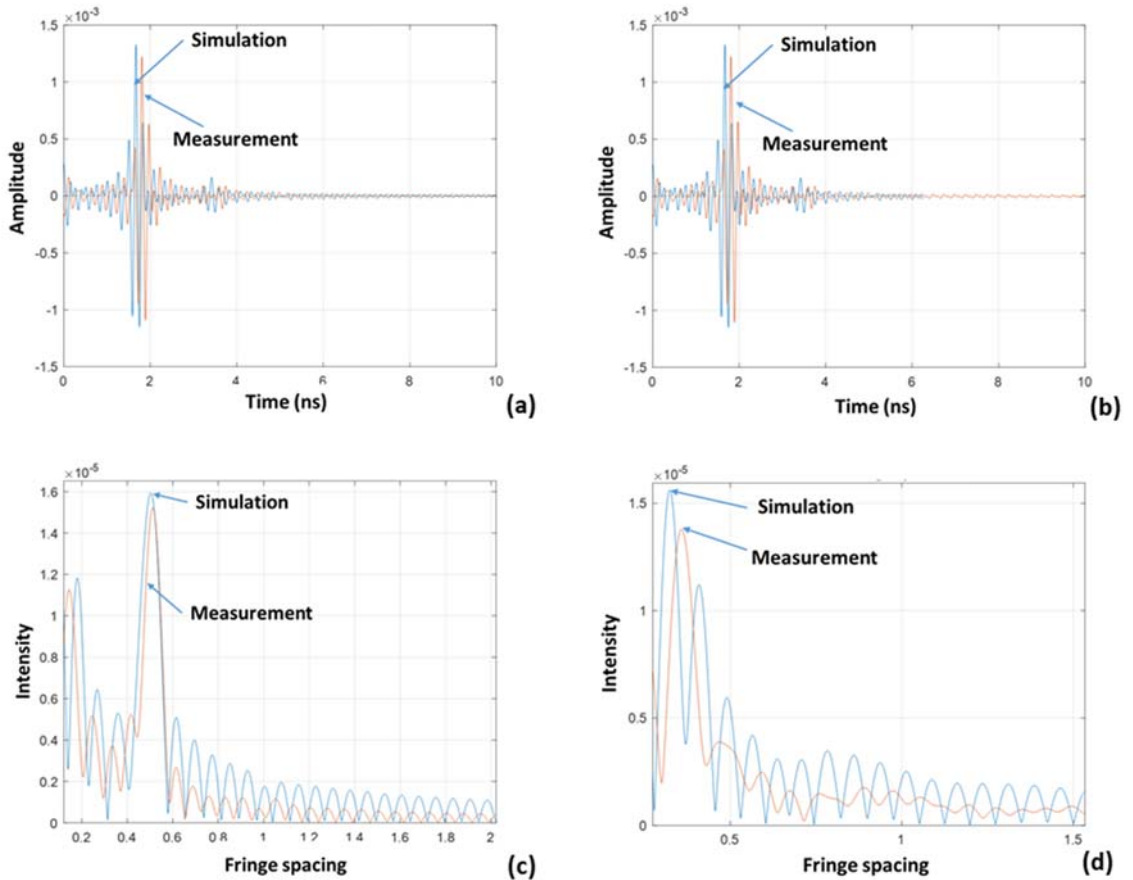

Figure 17: time domain reflection signal of the transmission line (a) with and (b) without the slit and fringe spacing of time-domain signal reflected by the transmission line with slit; (c) with time gating between 0 ns and 1.9 ns and (d) with time-gating between 0 ns and 1.26 ns.

generated by the transmission line with a slit is very similar to that without the slit because the reflection generated by the slit is much smaller in amplitude compared to the reflection generated by the end of the transmission line. The effect of the slit, however, can be clearly identified from the FFT of the fringe spectrum. As shown in Figure 17(c), when the time domain signal is time-gated between 0 ns and 1.9 ns, two peaks were observed; one correspond to the cavity between the input port and the end of the transmission line and the other corresponds to the cavity between the slit and the end. The peak corresponding to the cavity between the port and the slit was not visible because the small reflection at the slit is overwhelmed by the large reflection at the end of the transmission line. Change the time-gate from 0 ns to 1.26 ns, however, removes the reflection at the end of the transmission line. As a result, the spectrum of the time-gated fringe spectrum shows a dominate peak that corresponds to the cavity distance between the port and the slit, as shown in Figure 17(d).

Accomplishment #7: Improved and de-bugged the prosthetic interface control hardware/software and tested the data acquisition system to improve the precision of the recorded and displayed pressure value within each gait cycle

• **Specific objectives:**
1) Address issues related to the selective inflation, recording as well as improve the precision of the recorded and displayed values
2) Perform testing to assess the efficacy of the aforementioned fixes and determine system reliability by conducting pressure mapping and selective pressure modulation tasks with a healthy volunteer wearing the prosthetic interface
3) Implement a multi-color pressure mapping display to improve data visualization
4) Correct timestamp recordings for better association of the actuator pressure at particular instance of time
5) Perform pressure mapping and modulation tasks by conducting walking test with a healthy volunteer to evaluate the rectified timestamps and additional capabilities

• **Major activities**:
1) <u>Improvements and function corrections of the control unit</u>
   a. Modification of the GUI to provide more functionality: two additional buttons 'Test Start' and 'Test Stop' were added to aid the data collection during each test. Pressing the 'Test Start' button starts recording data into a separate file. The name of the file is decided based on the file name provided by the user. Every time the 'Test Start' button is pressed, a new file is created with a new number appended to the file name provided by the user. The 'Test Stop' button saves the recorded data into the file and appends any further data into the initial file name provided by the user. For example, if the file name provided using 'Change File' button is 'Test', then the subsequent files created upon pressing the 'Test Start' button will be 'Test1', 'Test2', and 'Test3' and so on until file name is changed again. And when the 'Test Stop' button is pressed the file name will revert to the default file name of "MyTest" (Figure 18). This improvement will help data gathering during continuous multiple test runs.
   b. An actuator selectivity option was added to allow the user a choice of which actuators to inflate when the system is commanded to modulate the internal pressure to a set pressure. This improvement solved a previous issue where certain solenoid valves would open unintentionally while the pressure value for other targeted actuators was updating. A benchtop test, as shown in Figure 19, was conducted where actuator 20 was selected and commanded an inflation pressure of 13.8kPa. The inflation of the selected actuator 20 opened only the corresponding solenoid valve and didn't modify the internal pressure of any other actuator. This verified the improvement in the actuator selectivity option.
   c. The precision of the displayed values was increased to two decimal points as can be seen in the GUI. This improvement was also extended to the recorded values. An error that occurred generating

a timestamp for the recorded data was corrected. This error would occasionally result in multiple recordings for the same timestamp.

d. A 7-color spectrum based color gradient was added to allow better data visualization. Other minor improvements such as increasing the font size and changing the data display font from white to black were also incorporated in the GUI.

e. The timestamp corresponding to each data set was collected directly at the microcontroller interface in order to correct an issue with timestamp capturing where multiple timestamps of the same value appeared for consecutive datasets.
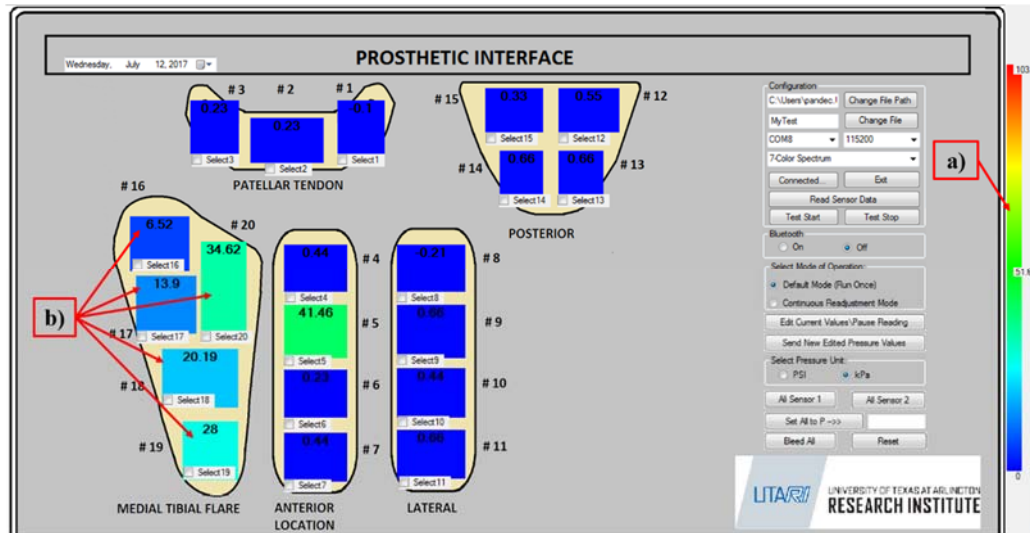

Figure 18: graphical User Interface (GUI) a) depicting a 7-color spectrum with Blue representing 0 kPa and Red representing 103.35 kPa, and b) presenting the multi-color mapping of the medial actuator as pressure is modulated to 6.8, 14, 21, 28, and 34 kPa, respectively

2) Preliminary benchtop testing to validate the stability and repeatability of the data acquisitions while an actuator is under dynamic loading cycles

a. The improved functionality of the system, including actuator selectivity and increased recording precision, was tested by repeatedly compressing a targeted actuator (actuator 20). The actuator was initially inflated at 13.8kPa and the internal peak pressure increased by pressing the actuator by hand. The peak pressure under compression was between 30-45kPa. As seen in Figure 19, the internal pressure value of the actuator was able to return to its starting value after each compression. This verified stability and repeatability of the data acquisition system as well as the dynamic
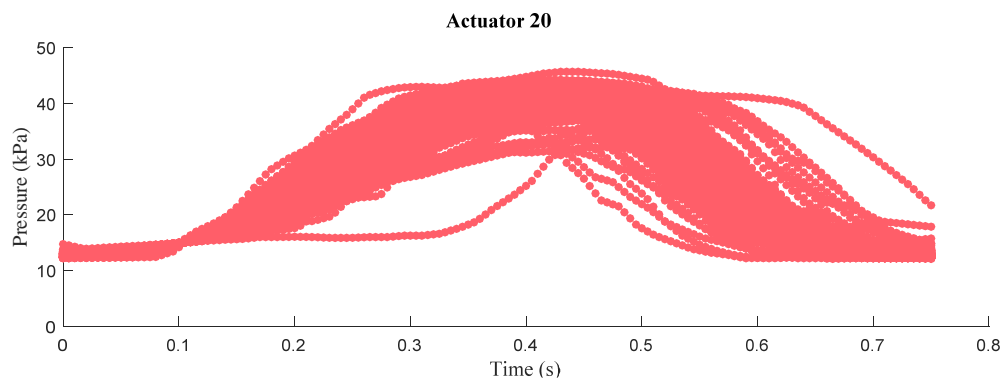

Figure 19: the overlaid internal pressure change of actuator 20 during a series of repeated compression and release loading

16

response of the actuator. The verified system will help to continuously capture the actuator internal pressure changes within each gait cycle.

    b. The regression test was performed to verify that the previous capabilities of the system remained intact and that the system could still continually monitor and modulate the internal pressure of the actuators. This verified that the modifications in the control system had not unintentionally changed the system's functionality.

3) <u>Reliability and load testing of the control system and the actuators</u>

    a. Performed walking test using a custom made Patella Tendon Bearing-Ankle Foot Orthosis (PTB-AFO) device with a prosthetic liner which is used to mimic the substrate of the interface pressure sensor. The PTB-AFO device was worn by a team member who performed walking at a constant speed (2miles/hr) on a treadmill. To investigate the significance of pressure modulation of individual and group of actuators, a series of tests were conducted. Before modulating a selected actuator or a group of actuators, a baseline of internal pressure of all actuators were obtained in order to compare before and after the pressure modulation. The actuators were all inflated to a constant pressure of 41kPa after wearing the device while no body weight exerted on the leg. Internal pressure of all actuators were recorded during walking to set a baseline before modulating the selected actuators. Then the test was repeated without inflating the selected actuator or actuators to investigate the internal pressure change of surrounding actuators in the same area.

    b. All the recorded internal pressure data taken during each walking test were plotted.

- **Significant Results:**

1) Data acquisition rate was increased to about 110 Hz with two decimals which allows for sufficient pressure data collection within each gait cycle. This further helped in an instantaneous identification of heel-strike and toe-off positions as well as actuator reactions at various load-bearing areas during walking.

2) The recordings from the tests initially conducted had a few errors in the timestamps. These inaccuracies were removed by acquiring the timestamps using the microcontroller at the same time when it is instructed to acquire the actuator internal pressure. This assured the correct association of actuator pressure at the given time.

3) During pressure modulation from selected actuators, an issue of unintentional opening of additional solenoid valves was identified and corrected. This provided an improved and reliable actuator selectivity function.

4) An increased precision was incorporated in the actuator internal pressure recordings to allow minute changes within the collected data to be recorded. This helped in capturing the changes in the actuator internal pressure recordings even with the presence of a gel liner in between the actuator and the limb which was found to heavily dampen the interface pressure between the actuators and the limb while walking.

5) The actuators and control system performed successfully during a continuous three-hour test when a health volunteer was walking on the treadmill. The system was commanded to re-inflate the actuator array over 100 times throughout the course of this test.

6) The pressure modulation tests results will be demonstrated in this section. All actuators 16-20 in the medial area were initially inflated to 41kPa. Then the selected actuators 16, 17, and 20 were decreased to 4 kPa while no pressure modulation was applied to the remaining actuators. Figure 20 shows a segment of the recorded pressure of all actuators over a duration of 20 s after pressure modulation. The pressure changes within each actuator clearly shows the repeated gait pattern. The internal pressure of the actuators 18 and 19 increased about 10% of the initial inflation pressure during each gait cycle. The modulated actuators still experienced a small amount of load from the leg during walking, however, the magnitude of the pressure and pressure variation was very small compared to the major load bearing actuators 18 and 19. This indicates that the remaining inflated actuators were being over compressed by the limb so that the modulated actuators were still in contact with the limb.
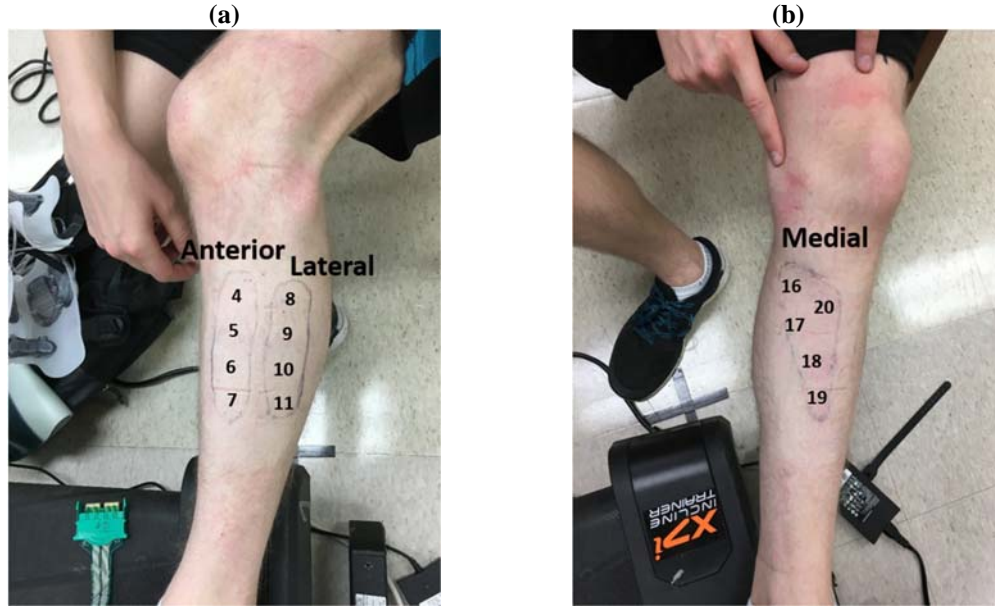
17

Figure 20: annotated locations of each actuator on the limb of the healthy volunteer.
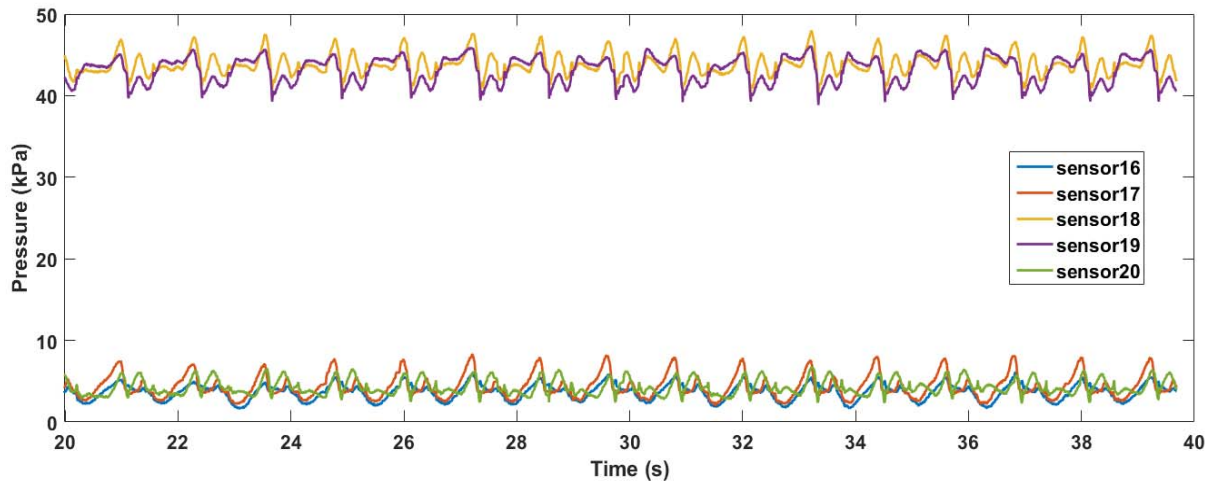

Figure 21: internal pressure plotted after decreasing internal pressure of actuators 16, 17, and 20 to 4kPa in medial area

Accomplishment #8: 1) Tested the improved data acquisition in internal pressure modulation while recording the corresponding interface pressure; 2) obtained the pressure trajectory for the load bearing areas within each step while the volunteer wore a prosthetic liner with the PTB-AFO device during walking

• **Specific objectives:** validate the pressure mapping and modulation capabilities of the actuators in the presence of a gel liner

• **Major activities**:

1) Performed walking test using the PTB-AFO device with a prosthetic liner and commercial interface pressure sensors. The PTB-AFO device was worn by a team member who performed walking at a constant speed (2 miles/hr) on a treadmill. The gel liner substitutes as the surface on which the interface pressure/shear sensor (still under development) will be embedded onto and also acts as a damping layer between the pressure actuator array and the limb. To examine the interface pressure modulation capability of the actuators when in contact with the gel liner, the commercially available F-Socket
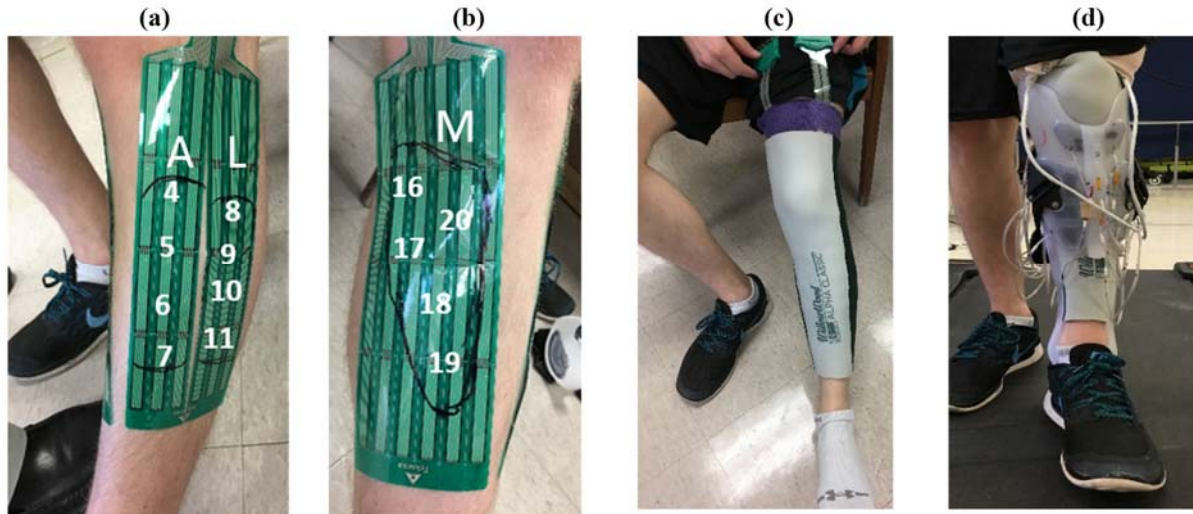
Figure 22: (a), (b) F-Socket sensors taped to the volunteer's limb, (c) the gel liner worn over the F-Socket sensors, and (d) the PTB-AFO device worn over the gel liner

sensor system was used to map the interface pressure at the locations corresponding with each pressure actuator patch. As seen in Figure 22(a) and (b), the F-Socket sensors were attached to the anterior, lateral, and medial locations of the leg using double-sided tape to ensure no-slippage occurred during walking. In the fitting process, the outline of the pressure actuator patches was imprinted onto the F-Socket sensor directly by wearing the PTB-AFO device while the patches were coated in wet marker ink. This allowed us to identify the sensing area corresponding to each air pressure actuator patch. A prosthetic gel liner, seen in Figure 22(c), was worn over the F-Socket sensor. The PTB-AFO with integrated pressure actuator array was worn over the gel liner, shown in Figure 22(d). To test the pressure modulation capability of the air pressure actuators, internal and interface pressure data were recorded simultaneously while the volunteer walked at a constant speed of 2 miles/hr on a treadmill for a duration of 2 minutes per test. Before investigating the consequence of modulating selected actuators, a baseline pressure of all actuators was obtained by collecting internal and interface pressure data while all actuators were initially inflated to a constant pressure of 46kPa. The test was then repeated by reducing pressure from selected actuators and actuator groups to compare both internal and interface pressures to the baseline pressure at the anterior, lateral, and medial areas, respectively.

- **Significant Results:**

1) The pressure trajectory baselines of the interface pressure in the anterior, lateral, and medial areas were calculated using the average contact pressure in each area. Similarly, the internal pressure trajectory baselines for these regions were calculated using the air pressure actuators' internal pressure values. In both cases, a MATLAB script was used to perform said calculations. The average contact pressure across these areas was provided by the F-Socket software whereas the corresponding average internal pressure was calculated by averaging the value of each actuator within that area. For a clear comparison between each test, the pressure trajectory of every step within a test was plotted to show the mean pressure and standard deviation over time. The mean pressure was plotted as a solid line and the standard deviation was shown in the shaded area. The baselines for interface and internal pressure were shown in Figure 23 (a)-(c) and (d)-(f), respectively. Due to the dampening and cushioning effects of the gel liner, the interface pressure fluctuates unsteadily within each step in all three areas shown in Figure 23(a)-(c), particularly in the lateral area (Figure 23(b)). In the lateral area, the contact between the limb and the actuators was not held continuously throughout each step, as seen in Figure 23(b),
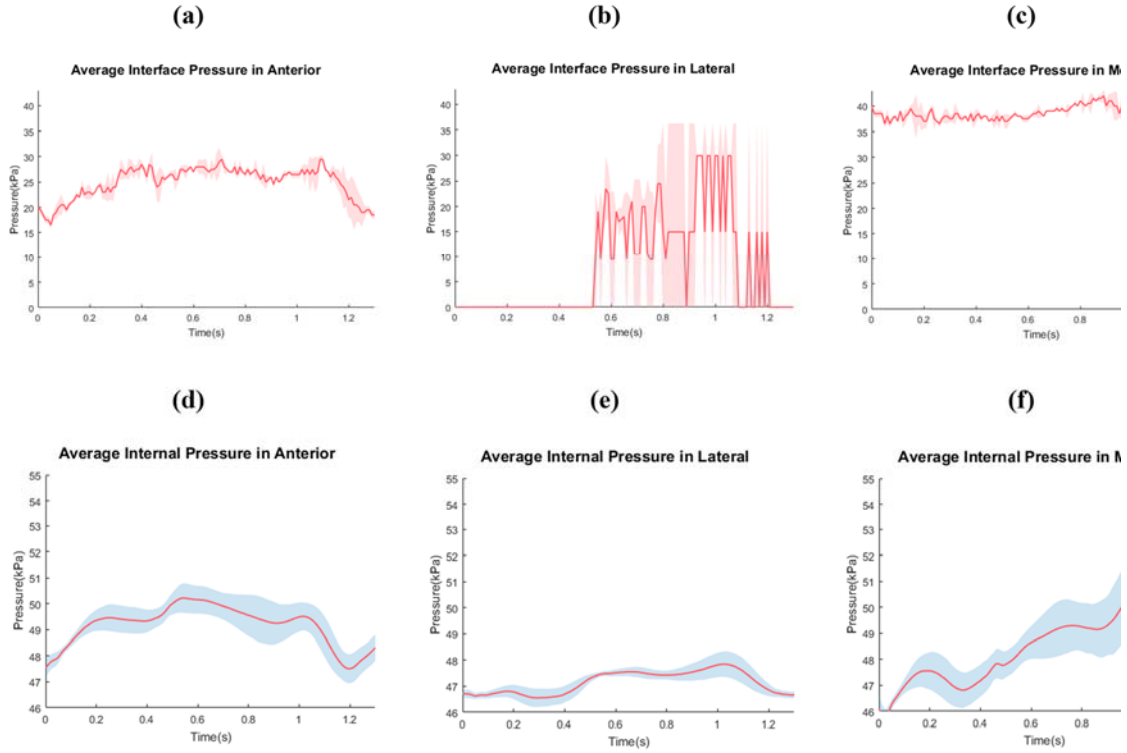
19

Figure 23: baseline of the average interface and internal pressure trajectory within steps when all actuators are inflated to 46kPa during walking

which is reflected in the insignificant internal pressure change shown in Figure 23(e). The medial area experienced slightly higher pressure than the anterior area and the corresponding internal pressure in the medial area also shows large changes.

2) In the first test, the pressure of selected actuators 16, 17, and 20 at the proximal end of the medial area was reduced to 4 kPa while keeping all other actuators at their inflation pressure of 46 kPa before walking. The averaged internal pressure in the remaining actuators 18, 19 of the medial area (Figure 24(f)) increased compared to the baseline (Figure 23(f)) since the average contact area was reduced from 38.71 cm^2 to 22.58 cm^2 and subsequently the load was shifted to the remaining actuators. As a result, the corresponding interface pressure, Figure 7(c), also showed a slight increase in comparison with the baseline seen in Figure 23(c), which indicates the interface pressure of a selected area can be removed or reduced through internal pressure modulation of a corresponding actuator or group of actuators. As expected, the pressure change in the lateral area is insignificant in both interface and internal pressure, shown in Figure 24(b) and 24(e). In the second test, pressure in actuators 4 and 5 at the proximal end of the anterior patch was reduced to 4 kPa. The average contact area was reduced from 22.58 cm^2 to 9.68 cm^2. However, neither the average interface pressure nor the average internal pressure showed a significant change (Figure 25(a) and (d)) in comparison to the baseline interface and internal pressures (Figure 23(a) and (d)) which implies that the load was shifted off of this area to other areas of the limb. This is seen to be the case as shown in Figure 25(b) where an increase in the constant contact in the lateral area, which is adjacent to the anterior, occurs.
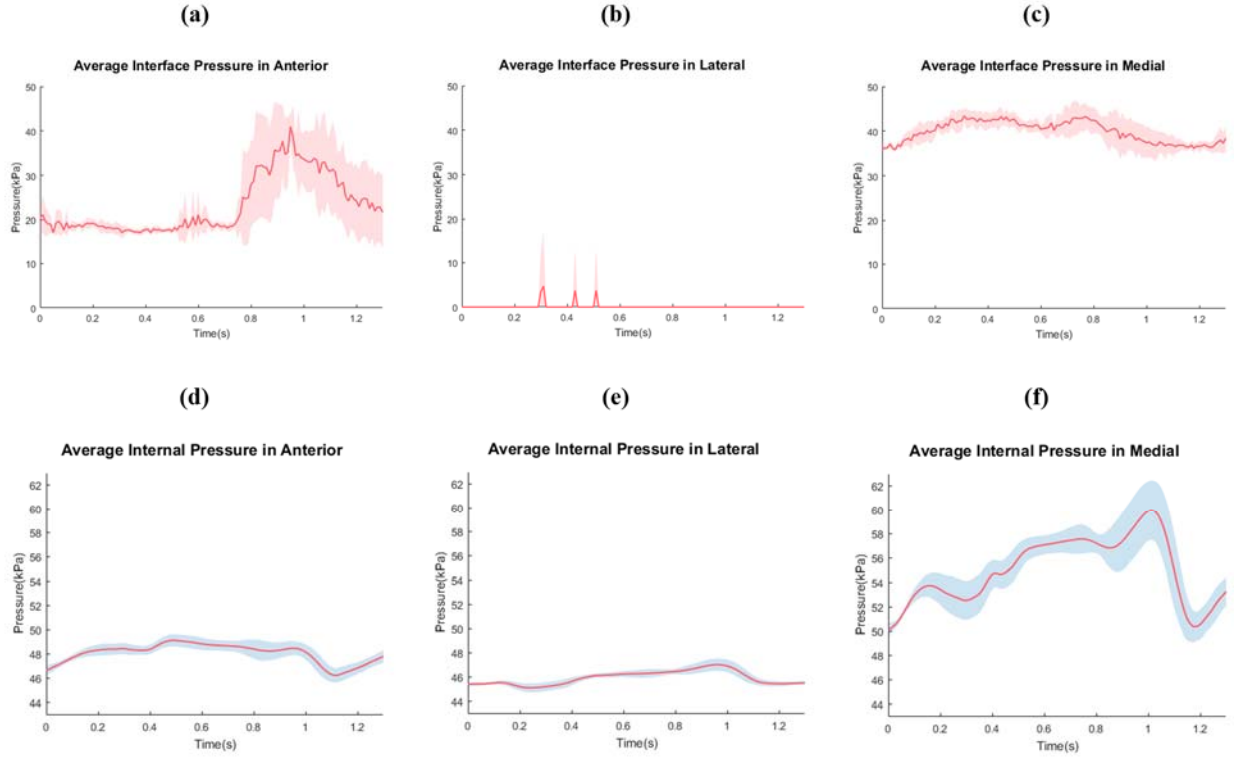
Figure 24: interface and internal pressure trajectory when actuators 16, 17, and 20 are modulated.
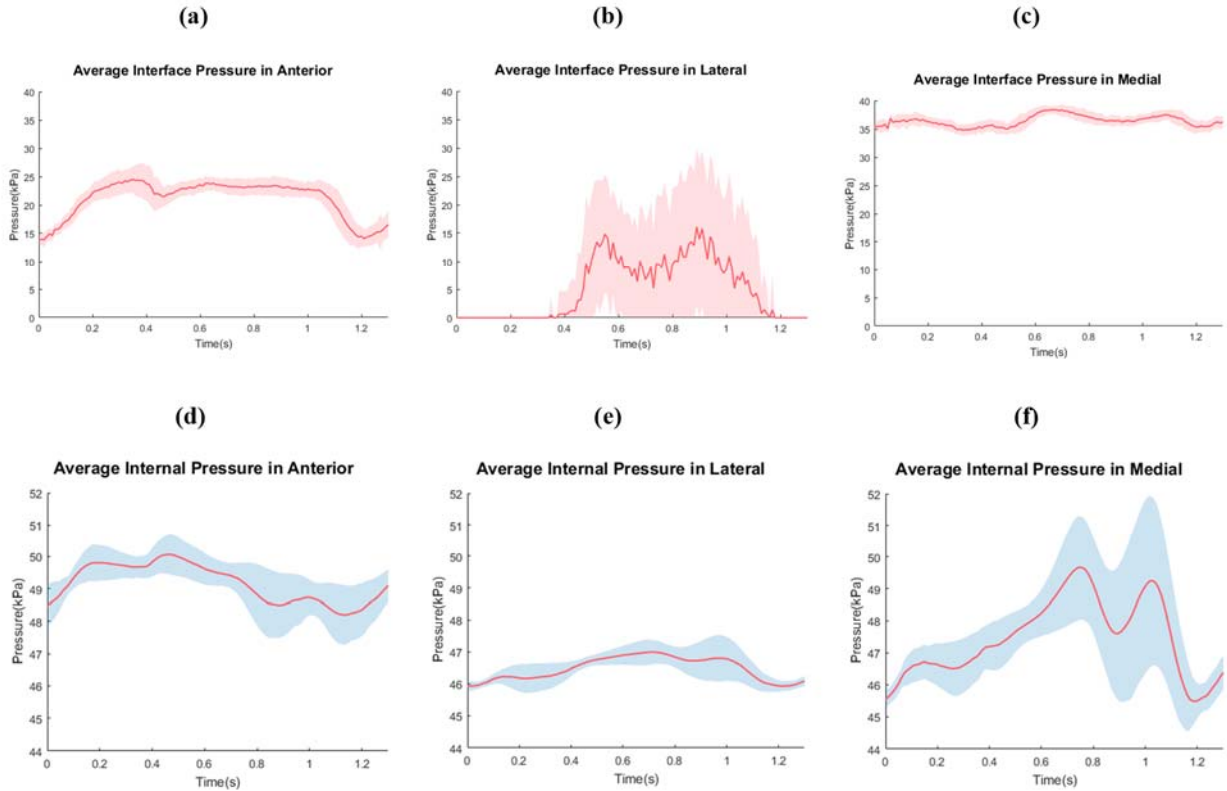

Figure 25: interface and internal pressure trajectory when actuators 4 and 5 are modulated.

Accomplishment #9: designed and built a working miniaturized control unit that is about 63.5% (3.08 lb compared to the previous version of 4.85 lb) in weight and 56% (6''x6''x5'' compared to 10''x8''x4'' in the previous version) in volume of the previous control unit.

- **Specific objectives:** reduce the size, weight, and cost of the existing control unit to improve the usability and portability of the device.

- **Major Activities:**

1) Control system design and prototyping: the control system consists of modules including an array of sensors, an array of solenoids mounted on the manifolds, an air pump, a power supply, and LEDs. Compared to the previous control system, the pressure regulator was removed. Instead, a solenoid valve mounted on a single-position manifold integrated with a pressure sensor is added in line with the air pump to facilitate pressure regulation. These modules are continuously monitored and controlled by a microcontroller either directly or over a SPI (Serial Peripheral Interface) protocol. A surface mount analog multiplexer is used to serially transfer the pressure sensor values over to the microcontroller and surface mount low-side switches are used to control the switching of the solenoids. Both of these operations are carried out in a master-slave configuration over the SPI protocol. A schematic circuit of the connections for these modules was drawn in EAGLE PCB design software to develop a PCB layout as shown in Figure 26. During the design process, schematic symbols and PCB footprints for each component were created as necessary. The components were laid out and routed to reduce the overall space and effectively utilize blank spaces. The blank spaces across the layout were made into prototyping areas to allow for any ongoing changes or replacements on the PCB. The schematic and layout were electrically verified using Electrical Rule Check and Design Rule Check functions, respectively, built in the PCB CAD software. The design was also reviewed by peers to check for any obvious errors and to suggest improvements. The final design of the board resulted in a PCB with an approximate dimension of 5.284" x 5.500" and encompassed each module with the exclusion of the pump and solenoids that were to be mounted on the inner side of the lid of enclosure as peripheral devices.

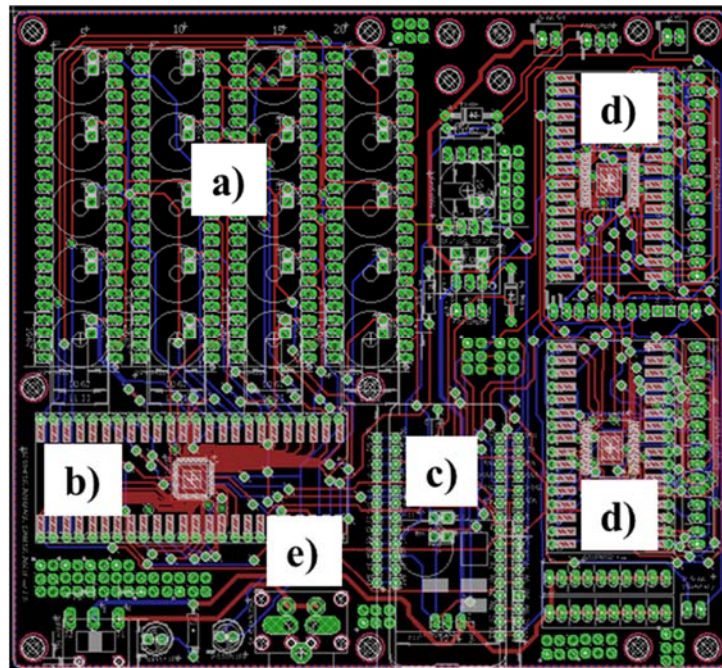Figure 26: PCB layout designed in EAGLE PCB design software showing a) pressure sensor arrays, b) analog input multiplexer, c) microcontroller section, d) solenoid switching section, e) main power supply

2) Circuit assembly and system integration: the PCB layout design files were submitted to a manufacturer (4pcb.com) to obtain a set of finished circuit boards (Figure 27 (a)). As shown in Figure 28(b), the SMT

and through-hole components required according to the design were hand soldered onto the board. Female and male headers were soldered to the board so that solenoids, pressure sensors, microcontroller board, and voltage regulators could be plugged into the board in order to allow these costlier components to be reused or troubleshoot should the board fail.

(a) **(b)**
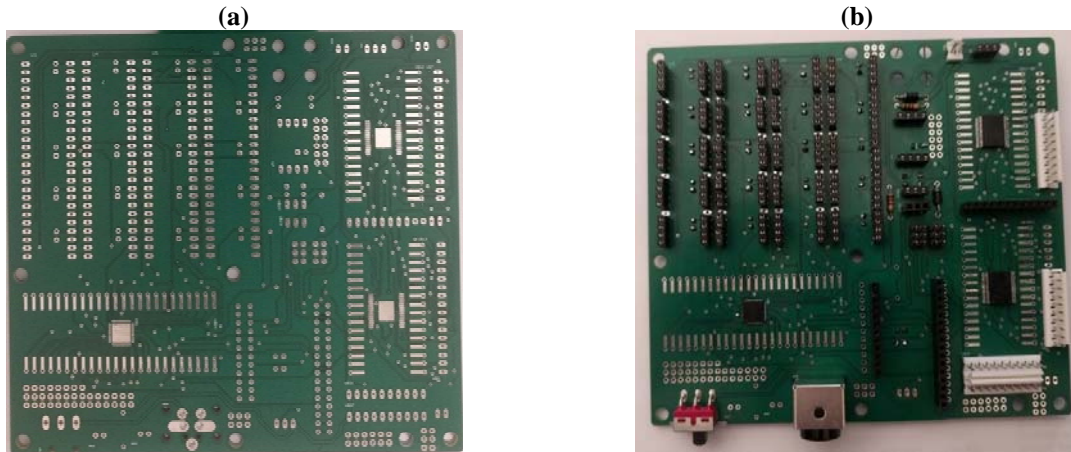
Figure 27: (a) manufactured PCB showing tracks and pads for through-hole and SMT (Surface Mount Technology) components, (b) PCB with SMT and through-hole components soldered in place
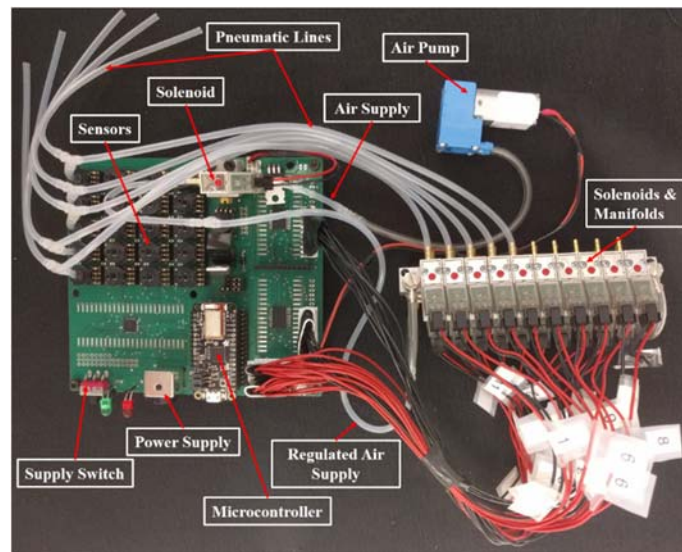
Figure 28: control system depicting the circuit board with all the components integrated and assembled including a microcontroller, an assembly of sensors, solenoids on manifolds and an air pump
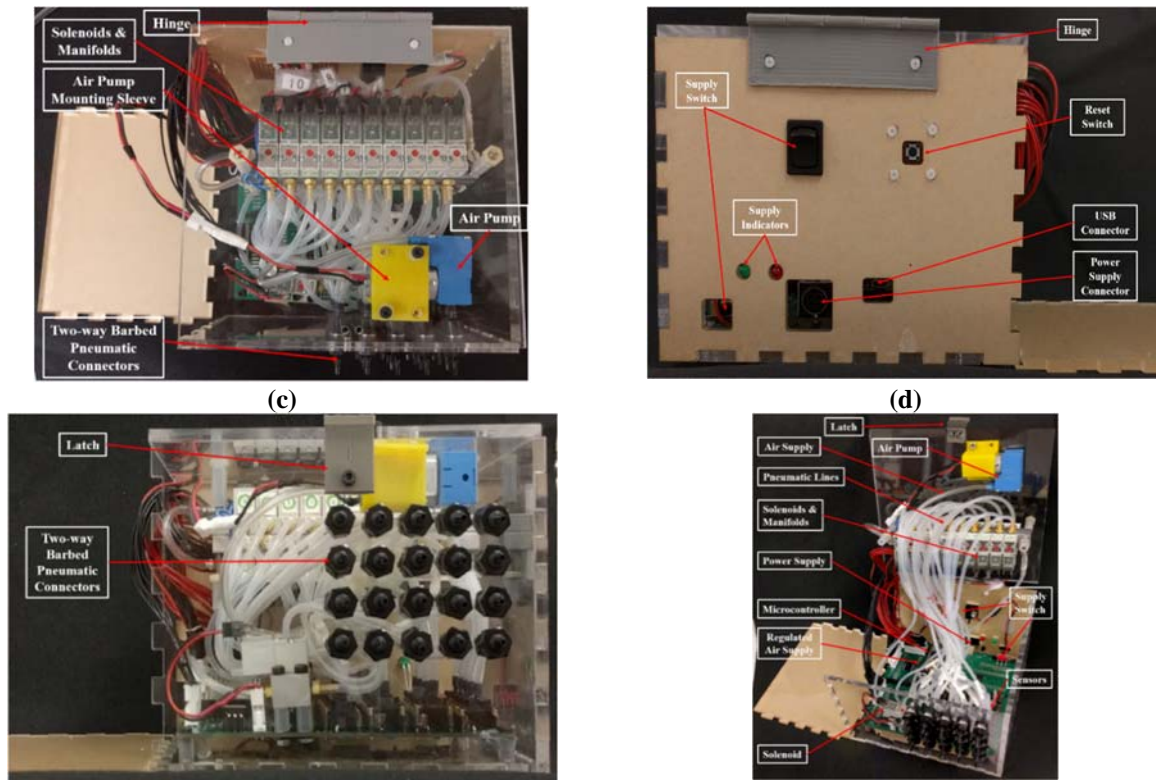
(a) **(b)**

Figure 29: control system packaged within an acrylic enclosure, (a) top view of the enclosure showing the air pump and the solenoids mounted on the inner side of the enclosure lid, (b) side view depicting the power supply side of the control unit with connections for power supply, reset switch, supply indicators and USB, (c) another side view showing the two-sided pneumatic barbed connectors for pneumatic connection for the actuators in the socket, (d) prospective view depicting the integration of the circuit board and the peripheral devices with the enclosure as well as showing a latch to open and close the top lid (the front plate is kept open to give additional room for debugging)

3) Module and system testing: individual circuit modules were tested before integration with the system as a whole. The module tests resulted in making a few connections such as input supply to one of the sensors. The system testing confirmed the working functions of the system and no further corrections were found to be necessary.

4) Control unit packaging: an enclosure was designed and built using 3/16'' thick acrylic sheet to house the assembled circuit board and the peripheral devices. The peripheral air pump and the solenoids together with manifolds were mounted onto the inner lid of the enclosure and connected to the board through terminal block connectors, seen in Figure 29(a). The air pump was mounted using a vibration dampening mounting sleeve to reduce wear on the acrylic enclosure. The enclosure has a supply side, as shown in Figure 29(b), to provide the power supply and USB connections, and to support the switch buttons and supply LEDs. The solenoid valves and the corresponding pressure sensors were connected using T-connectors. An array of two-sided barbed pneumatic connectors were mounted on one side of the enclosure to support the sensing and modulation of the actuators in the socket as shown is Figure 29(a) and (c). Figure 29(d) shows the complete integration of the control unit. Three side plates were glued to the bottom plate of the enclosure and the lid was connected by a hinge to one side of the enclosure. One side plate is left unglued to give additional room for any future debugging, if necessary.

- **Significant Results:** the design and prototyping of the new control unit successfully reduced the size, cost, and weight of the initial control unit by using components with a smaller footprint, such as Feather

M0 Bluefruit in place of Arduino Mega 2560 microcontroller board, multiplexer ICs in place of MOSFET arrays and their supporting circuitry, as well as removing the pressure regulator device, and the Arduino muxshield.

1) The weight of the new control unit is about 36.5% less than the weight of the previous version. The previous control system and the enclosure weighed about 4.85lbs. The current control system weighs about 3.08lbs with the enclosure. However, the control system alone weighs 1.525lbs that indicates almost half of the weight is contributed by the acrylic enclosure. We will explore different enclosure design and material in the future to further reduce the weight of the control unit. The total weight of the control unit in the next iteration is estimated to be less than 2lbs.

2) The size of the new control unit has reduced from the initial size of 10"x8"x4" (approx.) to 6"x6"x5" (approx.). We were able to reduce the volume of the control unit by 43%. With the smaller footprint and less weight of the control unit, it provides the potential and possibility of carrying the control unit on the prosthetic pylon and the waist. By exploring miniature solenoid and other packaging method, the overall size of the control unit can be further reduced.

- **What opportunities for training and professional the development has the project provided?**

The project supported four graduate students and three research scientists. It offers a unique opportunity for the graduate students, the research scientists and the PIs to interact with medical researchers at UT Southwestern medical school and gain insights and knowledge related to prosthetics and orthopedics. A Masters student has graduated with the support of this grant and another Masters student is expected to graduate by the end of this year. An undergraduate minority student is participating in the project on the mechanical design of the test fixture and calibration of the cantilever beam load cells.

- **How were the results disseminated to communities of interest?**

A journal paper is published on line (DOI: 10.1109/JSEN.2017.2765893). The PI's group showcased the research at Department of Mechanical and Aerospace Engineering open house and at the Engineering Week event hosted by the College of Engineering at UTA.

- **What do you plan to do during the next reporting period to accomplish the goals?**
    1) Synchronize the data collected from the CBLCs and antenna sensor
    2) Characterize the antenna shear and pressure sensor fabricated on Denim
    3) Evaluate the microstrip Fabry-Perot resonator and T-resonator for bio-impedance measurement
    4) Conduct experimentation using the actuator integrated PTB-AFO device with interface pressure/shear antenna sensors
    5) Develop data transfer scheme from pressure/shear antenna sensors to the actuator control unit for close-loop control
    6) Continue development of the portable control system to include battery powered operation
    7) Explore different enclosure design and material to further reduce the weight of the control unit
    8) Perform clinical evaluation of the smart liner and active fitting mechanism

4   IMPACT
- **What was the impact on the development of the principal discipline(s) of the project?**

This project period achieved a major breakthrough in producing a robust antenna sensor that can be embedded in flexible prosthetic liner by 1) validating the functionality of the antenna sensor fabricated on textile material such as Denim; and 2) demonstrate wireless interrogation of the antenna sensor without a connector. The test apparatus and the associated data acquisition hardware/software could be very beneficial for future clinical testing to understand the interaction between the prosthetic socket and the residual limb.

- **What was the impact on other disciplines**

Flexible sensors have been studied for many different applications. Connection to the flexible sensors remains a challenge to produce hermetic and robust flexible sensors. Wireless interrogation of the antenna sensor without a connector is a promising solution to this challenge for other applications.

- **What was the impact on technology transfer?**

A US patent titled "Sensor assembly, method, and device for monitoring shear force and pressure on a structure" has been granted (#9138170 B2). UTA Technology Management Office has been actively seeking license opportunities for this technology.

- **What was the impact on society beyond science and technology?**

None to report.

5   CHANGES/PROBLEMS
- **Changes in approach and reasons for change**

Wireless interrogation of the antenna sensor without a connector, which was not original proposed, was added because the challenge of producing a robust antenna sensor with a connector.

- **Actual or anticipated problems or delays and actions or plans to resolve them**

A one-year no-cost extension has been approved to compensate for the delay due to difficulty in graduate students obtaining visas and large turnover of graduate students.

- **Changes that had a significant impact on expenditures**

Delay in hiring graduate students due to visa issues.

- **Significant changes in use or care of human subjects, vertebrate animals, biohazards, and/or select agents**

None.

6   PRODUCTS
- One journal paper published on line;
- Two conference papers;
- One Masters thesis;
- Project description at the PI's website (astl.uta.edu);
- One patent granted (US9138170 B2);
- A test apparatus that imitate the limb-socket interface;
- Wireless data acquisition system for smart socket and liner;
- A rapid prototyping technique to fabricate antenna sensor on textile materials;
- A miniaturized pneumatic control unit that can be used in the human subject testing
- Data acquisition system that can capture data at 110Hz for real-time control of the actuator that allows dynamic adjustment of the prosthetic fit
- A graphical user interface that allows for data visualization and control
- A Matlab script for retrospective analysis of the pressure data during the gait cycle

7   PARTICIPANTS & OTHER COLLABORATING ORGANIZATIONS
- **What individuals have worked on the project?**

  Name: Haiying Huang
  Project Role: PI
  Researcher Identifier (e.g. ORCID ID):

Nearest person month worked: 4
Contribution to Project: advice and assist students and research staff

Name: James Skilskyj
Project Role: Research staff
Researcher Identifier (e.g. ORCID ID):
Nearest person month worked: 12
Contribution to Project: Implement test apparatus, controller, control software
Fabricate and characterize antenna sensors

Name: Farnaz Farahanipad
Project Role: Graduate Research Assistance
Researcher Identifier (e.g. ORCID ID):
Nearest person month worked: 12
Contribution to Project: Characterize sensor performance
Investigate wireless interrogation scheme

Name: Elmira Ghahramani
Project Role: Volunteer (support with department teaching assistantship)
Researcher Identifier (e.g. ORCID ID):
Nearest person month worked: 1
Contribution to Project: Fabricate sensors

Name: Abhilash Tankasali
Project Role: Volunteer
Researcher Identifier (e.g. ORCID ID):
Nearest person month worked: 3
Contribution to Project: Investigate microstrip Fabry-Perot resonator

Name: Muthu Wijesundara
Project Role: Co-PI
Researcher Identifier (e.g. ORCID ID):
Nearest person month worked: 0.59
Contribution to Project: Provide the guidance on test design and configuration

Name: Wei Carrigan
Project Role: Researcher
Researcher Identifier (e.g. ORCID ID):
Nearest person month worked: 1.45
Contribution to Project: Built test setup and performed test and data analysis

Name: Caleb Nothnagle
Project Role: Researcher
Researcher Identifier (e.g. ORCID ID):
Nearest person month worked: 1.36
Contribution to Project: Conduct PTB-AFO testing,
Developed the control system programming and setup

Name: Manish Guar

Project Role: Student Intern
Researcher Identifier (e.g. ORCID ID):
Nearest person month worked: 1.5
Contribution to Project: Develop control system setup

- **Has there been a change in the active other support of the PD/PI(s) or senior/key personnel since the last reporting period?**
  Nothing to Report

- **What other organizations were involved as partners?**
  <u>Organization Name</u>: The Ohio Willow Wood Company
  <u>Location of Organization</u>: Mt. Sterling, Ohio
  <u>Partner's contribution to the project</u>: technical consultant

8   SPECIAL REPORTING REQUIREMENTS
  Quad chart (see appendix)

9   APPENDICES
  - Quad chart
  - One journal manuscript

Sensing and Dynamic Fitting for Enhanced Comfort and Performance of Prosthetics

OR130167
Award number: W81WXWH-14-1-0502

**PI:** Haiying Huang   **Org:** University of Texas Arlington **Award Amount:** $744,300

Study/Product Aim(s)

- Demonstrate real-time measurements of interface stresses and residual limb volume
- Produce active interfaces that can automatically adjust the fitting of the prosthetic socket
- Test the active prosthetic interface and the shear-based fitting strategy in clinical settings

Approach

We will develop a smart prosthetic interface consisting of two inserts; a sensor insert and an actuator insert. The sensor insert will contain pressure, shear, circumference, and bio-impedance sensors while the actuator insert will be equipped with vacuum suction ports and pressurized bubbles. A shear-based fitting strategy will be implemented to guide the automatic adjustment of the socket. The smart socket will be tested in clinical settings to evaluate the shear-based fitting strategy.

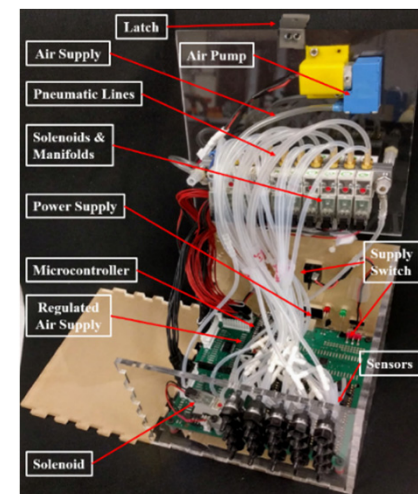**Instrumented Socket with wireless data acquisition systems**
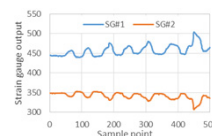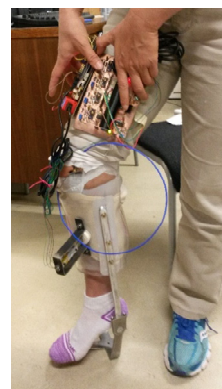
Strain gauges
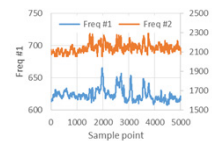
Antenna sensor

Miniaturized Control Unit

Timeline and Cost

Activities CY	14	15	16	17
Characterize sensor performance				
Demonstrate sensor insert				
Produce actuator inset				
Test smart socket in clinical settings				
Estimated Budget ($K)	**$50**	**$250**	**$250**	**$200**

Updated: 10/29/2017

Goals/Milestones

CY14 Goal – demonstrate simultaneous shear and pressure sensing
✓ Characterize sensor performance on test bed
✓ Design, fabricate, and characterize bubble actuators
CY15 Goals – realize sensor insert and actuator insert
☐ Investigate limb volume sensors
✓ Realize and characterize sensor insert
✓ Realize and characterize actuator insert
CY16 Goal – demonstrate smart socket
☐ Validate shear-based fitting strategy
☐ Conduct phase I clinical test
CY17 Goal – Conduct phase II clinical test
☐ Improve smart socket for phase II clinical test

Comments/Challenges/Issues/Concerns

- Actual expenditure may not be update due to complications related to accounting system changes

Budget Expenditure to Date
Projected Expenditure: $ 744,300
Actual Expenditure: $ 508,109

A Stacked Dual-Frequency Microstrip Patch Antenna for Simultaneous Shear and Pressure Displacement Sensing

Haiying Huang, *Member, IEEE,* F. Farahanipad, and A. K. Singh

Abstract—This paper presents a simultaneous shear and pressure displacement sensor based on the microstrip patch antenna technology. The antenna sensor consists of a dual-frequency patch antenna, a superstrate, and a rectangular director. The two fundamental resonant frequencies of the patch antenna are influenced by the lateral and vertical positions of the director with respect to its radiation patch. Therefore, the shear and pressure displacements of the director can be determined simultaneously from two fundamental antenna resonant frequencies. The antenna sensor was designed, fabricated, and tested to characterize its sensing performance. An algorithm was developed to inversely determine the shear and pressure displacements from the measured antenna frequencies. We validated that the typical measurement uncertainties of the antenna sensor is ± 0.3 mm for the shear displacement and ± 0.15mm for the pressure displacement. The presented shear/pressure displacement sensor is intended for monitoring the interaction between the human body and assistive medical devices (*e.g.* prosthetic liners, diabetic shoes, seat cushions *etc.*)

Index Terms— Shear and pressure sensor, microstrip patch antenna, pressure ulcer, prosthetic socket, diabetics, robots, tactile sensor

I. Introduction

TWO types of forces exist at the interface between two objects when they interact with each other; the force that is perpendicular to the interface is called the pressure force, while the force that is parallel to the interface is called the shear force. Measuring these two interfacial forces is crucial for many applications. For example, the human hand has the capability of perceiving the pressure as well as the shear forces, which enables us to detect slippage and the texture of objects [1]. Recently, there are increasing interests in developing tactile sensors for robots that can imitate the tactile sensation of human hands [2]–[5]. The combination of the shear and pressure forces is also believed to play important roles in the ulceration of tissues, which has plagued the populations with diabetics [6][7], wheel chair users [8], amputees [9], and those who wear assistive medical devices. Embedding shear and pressure sensors in wearable devices, such as diabetic shoes, seat cushions, prosthetic sockets, *etc.* will not only provide the needed guidance on how to adjust these devices for alleviating adverse conditions but also could provide an important instrument for studying the etiology of pressure ulcers.

Different physical mechanisms have been exploited in the past to realize simultaneous shear and pressure sensors. Most of these sensors measure displacements, from which the responses of the sensor to the shear and pressure forces are determined through calibration. Strain gauges were first used for shear and pressure measurements at the interface of a residual limb and a prosthetic socket [10]. Later, micro-machining technologies were introduced to reduce the sensor size and to improve the spatial resolution, in which the strain gauges were replaced by other piezoresistive sensing elements [11]–[13]. One drawback of the piezoresistive sensors is that their resistance changes are typically very small and thus require delicate signal conditioning. The high power consumption of these sensors could also prevent them from being used in battery-powered portable monitoring systems. Shear and pressure sensing using capacitor arrays have been studied by several researchers [4], [14]–[16]. In addition to being sensitive and power efficient, capacitive sensors can be implemented in flexible membranes and thus are more compatible with the human skin. Capacitive sensors, on the other hand, are sensitive to temperature and humidity. In comparison, optoelectronic sensors, which detect displacements based on the light coupling between a light emitting diode (LED) and a photo detector, are insensitive to environmental effects and thus can provide robust measurements [5], [17], [18]. Inductive sensors have also been investigated to address the environmental sensitivity issues as well [19].

In order to measure shear and pressure displacements simultaneously, the aforementioned sensors usually have multiple sensor elements; each sensor element needs one pair of wire for signal transmission. Some sensor elements may also require additional wiring for power. As a result, such a sensor could have a dozen wires connected to it. This large wire count severely limits the number of sensors that can be implemented in a distributed fashion. Multiple optical fiber sensors, on the other hand, can be implemented in one strand of optical fiber

H. Huang, F. Farahanipad, and A.K.Singh are with the University of Texas Arlington, Dept. of Mechanical and Aerospace Engineering, Arlington, TX 76019 (e-mails: huang@uta.edu, farnaz.farahanipad@mavs.uta.edu, abhay.singh@mavs.uta.edu).

and thus have been studied for distributed shear and pressure sensing [20]–[22]. Unfortunately, the interrogation instruments for optical fiber sensors are usually quite bulky and expensive. Another class of sensors that can enable distributed sensing is the electromagnetic (EM) resonant sensor [23]–[28]. Not only can these sensors be configured to sense multiple modalities simultaneously, they also can be interrogated using wireless means. Microwave patch antenna sensor is such an EM resonant sensor [29], [30]. Previously, the authors' group has studied a patch antenna for shear measurements [31]. The patch antenna was combined with a loop antenna for simultaneous shear and pressure sensing [32]. Even though frequency division multiplexing can be exploited for interrogating multiple antenna sensors using wireless means [33], [34], connecting these two antennas to a single transmission line could be very challenging since they were stacked vertically instead of residing in the same plane.

In this paper, we present a single antenna sensor for simultaneous shear and pressure displacement measurements. The antenna consists of a dual-frequency patch antenna and a director separated from the antenna using a superstrate. The shear and pressure displacements between the radiation patch and the director cause the two antenna resonant frequencies to shift. Establishing the relationships between these two sets of parameters thus enables us to inversely determine the shear/pressure displacements from the measured antenna frequencies. Since the resonant frequencies of the antenna sensor can be acquired using a single microstrip transmission line, it has a very simple configuration and can be easily multiplexed to form distributed wireless sensor arrays.

II. Principle of Operation

The simultaneous shear and pressure displacement sensor is essentially a stacked microstrip patch antenna consisting of a regular patch antenna, a superstrate, and a director, as illustrated in Fig. 1(a). Functioning as an EM resonator, the regular microstrip patch antenna receives or radiates EM signals at its resonant frequencies. A regular microstrip patch antenna usually consists of three components, namely a radiation patch, a dielectric substrate, and a ground plane. When a broadband EM signal is supplied to the radiation patch through a microstrip transmission line, the signal whose frequency matches the antenna resonant frequency is radiated by the radiation patch while the remaining signal is reflected back. The spectrum of the reflected signal, therefore, displays significant losses at the antenna resonant frequencies. This phenomenon is represented by a S11 curve that plots the return loss of the patch antenna as a function of the incident frequency, as shown in Fig. 1(b). The fundamental antenna resonant frequencies are identified as the frequencies at which the return loss is a local minimum. With a rectangular radiation patch, the microstrip patch antenna has two fundamental resonances. The TM_{10} resonance has current flow along the length direction of the radiation patch while the TM_{01} mode has current flow along the width direction. Based on the transmission line model [35], the resonant frequencies of a microstrip patch antenna are determined by the dimensions of the radiation patch and its effective dielectric constant ε_{re} as

$$f_{mn} = \frac{c}{2\pi\sqrt{\varepsilon_{re}}}\sqrt{\left(\frac{m\pi}{L}\right)^2 + \left(\frac{n\pi}{W}\right)^2}, \quad (1)$$

where c is the speed of light in vacuum, L is the length of the antenna patch, and W is the width of the antenna patch. f_{10} and f_{01} represent the resonant frequencies of the TM_{10} and TM_{01} resonances, respectively. For a microstrip patch antenna having air as its superstrate (i.e. the un-loaded antenna), its effective dielectric constant is approximately equal to the dielectric constant of the substrate. When a superstrate and a metallic director are placed on top of the radiation patch, the effective dielectric constant of the antenna is contributed by the dielectric constant of the superstrate as well [36]. In addition, the antenna resonant frequencies are also sensitive to the vertical and lateral positions of the director due to the EM coupling between the radiation patch and the director. A shear or pressure force applied on the sensor deforms the superstrate and thus changes the position of the director, which in turn shifts the antenna resonant frequencies. Measuring the two antenna resonant frequencies, therefore, enables deducing the shear and pressure displacements of the director simultaneously.

III. Sensor Design and Fabrication

The configuration of the antenna shear and pressure displacement sensor as well as its design parameters are shown in Fig. 2. A rectangular director was selected due to its simplicity. The director was chosen to be wider than the radiation patch so that a slight shift of the director along the width direction of the radiation patch does not have any effect on the antenna resonant frequencies (see Fig 2(a)). On the other hand, the director only covers a portion of the radiation patch along its length direction. The length direction of the radiation
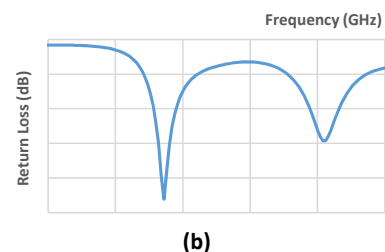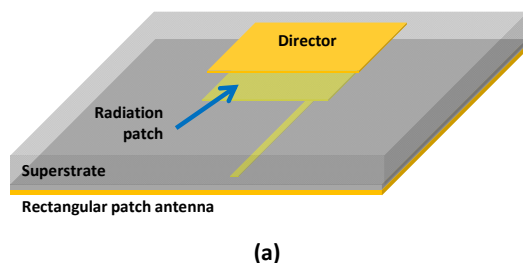
Fig. 1. A shear/pressure displacement sensor based on microstrip patch antenna technology; (a) sensor configuration; the rectangular patch antenna consists of a ground plane, a dielectric substrate, a microstrip transmission line, and a rectangular radiation patch. The director is separated from the radiation patch by a superstrate; (b) typical S11 curve of a dual-frequency microstrip patch antenna. The antenna resonant frequencies are determined as the frequency positions of the local minima.

Fig. 2. Configuration and design parameters of the antenna shear/pressure displacement sensor; (a) top view; (b) side view; the radiation patch is embedded between the substrate and superstrate; (c) director dimensions; (d) radiation patch and microstrip transmission line dimensions.

Fig. 3. Effect of superstrate dielectric constant on the antenna resonant frequency of a single-frequency patch antenna and the effective dielectric constant derived from the simulated antenna resonant frequency shift.

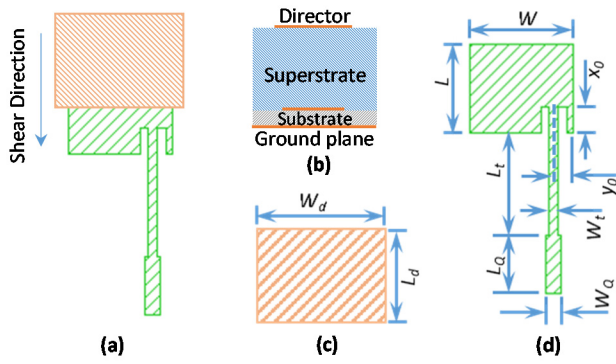patch is therefore the shear direction of the antenna sensor. The side view of the antenna sensor is shown in Fig. 2(b). The components with a solid golden fill (*i.e.* the ground plane, the radiation patch, and the director) are conductive while the components with a hatched fill (*i.e.* the substrate and superstrate) are dielectric materials. The design parameters include the dielectric constant ε_{r1} and thickness h_1 of the substrate, the length L and width W of the radiation patch, the dielectric constant ε_{r2} and height h_2 of the superstrate, as well as the shape, dimensions, and position of the director placed on top of the superstrate. In addition, the radiation patch will be fed by a microstrip transmission line terminated with a 50 Ω SubMiniature version A (SMA) connector to excite the resonance modes. In order to achieve impedance matching among the radiation patch, the microstrip transmission line, and the SMA connector, inset feeding and a quarter-wavelength (Q-λ) impedance transformer have to be designed. The design parameters for the feeding mechanism include the inset feeding location (x_0, y_0), the length L_t and width W_t of the microstrip transmission line, and the length L_Q and width W_Q of the Q-λ transformer. A commercial high frequency dielectric laminate with a dielectric constant of 3.48 and a thickness of 1.52 mm (RO4350B from Rogers Corp.) was selected as the substrate material. Silicone rubber, which is commonly used in commercial prosthetic liners, was selected as the superstrate material. The height of the superstrate was selected to be 5 mm, which is the typical thickness of prosthetic liners.

Since silicone rubber can vary widely in compositions, the dielectric constant of silicone rubber has to be characterized experimentally. For this purpose, a single-frequency patch antenna with a 5 mm thick superstrate, *i.e.* a superstrate-loaded antenna, was designed and modeled using an EM simulation tool (Sonnet Pro 16.52). The simulated antenna resonant frequency is plotted versus the superstrate dielectric constant in Fig. 3, which shows that the antenna resonant frequency reduced linearly with the increase of the superstrate dielectric constant. Based on the resonant frequency shifts, we can inversely determine the effective dielectric constant of the superstrate-loaded antenna from the f_{10} frequency [36], *i.e.*
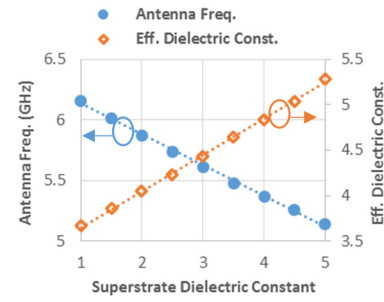
$$f_{10} = \frac{c}{2\sqrt{\varepsilon_{re}}\,L} . \tag{2}$$

The effective dielectric constant, calculated from the simulated antenna resonant frequency using (2), was 3.676 for the un-loaded antenna and it increases linearly with the superstrate dielectric constant, as shown in Fig. 3. The single-frequency patch antenna was fabricated from a substrate with double sided copper clad using a chemical etching technique. The frequency of the fabricated patch antenna was measured with and without the superstrate. Due to the variability associated with the fabrication process, the fabricated antenna without the superstrate had a resonant frequency of 5.96 GHz, while the simulated resonant frequency was 6.16 GHz. The difference between the simulated and measured frequencies is around 3%. Placing the superstrate on top of the radiation patch shifted the antenna resonant frequency to 5.78 GHz. Due to the discrepancy between the simulated and measured antenna frequencies, the measured frequency cannot be used directly for obtaining the superstrate dielectric constant from Fig. 3. To compensate for the discrepancy, the effective dielectric constant of the silicone-loaded antenna was calculated using eq. (6) in [36], the measured antenna frequencies of the loaded and unloaded antenna (f_r = 5.78 GHz, f_{r0} = 5.96 GHz) and the effective dielectric constant of the unloaded antenna (ε_{r0} = 3.676), which resulted in an effective dielectric constant of 3.9 for the superstrate-loaded antenna. Based on the relationship between the superstrate dielectric constant and the effective dielectric constant of the superstrate-loaded antenna shown in Fig. 3, the dielectric constant of the silicone superstrate was then determined to be 1.63, which is much smaller than the values of between 3.0 to 4.0 reported in [37], [38]. We obtained similar dielectric constant values for a 2 mm thick superstrate and the 5 mm thick superstrate using a patch antenna with a much thinner substrate. In both cases, the simulation model was modified to reflect the thickness changes. Therefore, the smaller dielectric constant obtained is likely due to the composition of the prosthetic liner material, which is much softer than the silicone materials that are used for antenna Radomes.

Based on the literature review [6], the sensor size was chosen to be around 10 mm. Following the antenna design procedure described in [39], the f_{01} and f_{10} frequencies were selected to be 6 and 7 GHz, respectively, which resulted in a radiation patch
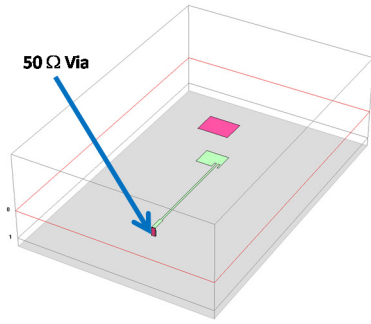
Fig. 4. Three-dimensional view of the antenna shear/pressure displacement sensor simulated using an electromagnetic simulation tool (Sonnet Pro 16.52).

of 12.1 mm in width and 10.2 mm in length. The width of the microstrip transmission line was chosen to be 1.0 mm, which has an impedance of 90 Ω for an effective dielectric constant of 3.9. The inset feeding location (x_0, y_0) was calculated accordingly using the approach described in [39]. Finally, the impedance of the Q-λ transformer was calculated as $Z_q = \sqrt{Z_{50} \times Z_t} = 67$ Ω, where Z_{50} represents the 50 Ω impedance of the SMA connector and $Z_t = 90$ Ω is the impedance of microstrip transmission line. The corresponding width and length of the Q-λ transformer are 1.9 mm and 6.7 mm, respectively. The width of the director was chosen to be 16 mm, which leaves a 2 mm margin on each side of the radiation patch along the width direction. As such, the antenna sensor is not sensitive to slight lateral movements of the director. The length of the director controls the sensitivities and overall size of the sensor, which in turn determines its spatial resolution; a shorter director results in lower sensitivities but a finer spatial resolution while a longer director leads to high sensitivities and

TABLE I
DESIGN PARAMETERS OF ANTENNA SHEAR AND PRESSURE
DISPLACEMENT SENSOR

Symbol	Quantity	Selected Values
ε_{r1}	substrate dielectric constant	3.48
h_1	substrate thickness	1.52 mm
ε_{r2}	superstrate dielectric constant	1.63
h_2	superstrate thickness	5.0 mm
ε_{re}	effective dielectric constant	3.90
L	radiation patch length	10.2 mm
W	radiation patch width	12.1 mm
L_t	transmission line length	50 mm
W_t	transmission line width	1 mm
L_Q	Q-λ transformer length	6.7 mm
W_Q	Q-λ transformer width	1.9 mm
L_d	director length	12 mm
W_d	director width	16 mm
(x_0, y_0)	transmission line feeding position	(2.2, 3.0) mm

a coarser spatial resolution. As a trade-off, the length of the director was chosen to be 12 mm.

The sensor design was modelled in Sonnet Pro. A three-dimensional (3D) view of the simulation model is shown in Fig. 4. The simulation box was 100 mm wide and 150 mm long with a cell size of 0.05 mm square, resulting in 2000X3000 cells in total. The top surface of the simulation box was assigned to be free space while the other five surfaces were assumed to be lossless metal. The space between the director and the top surface had a height of 10 mm and was filled with air. To excite the patch antenna, a square via with a dimension of 1 mm by 0.2 mm and a 50 Ω port were placed at the end of the microstrip
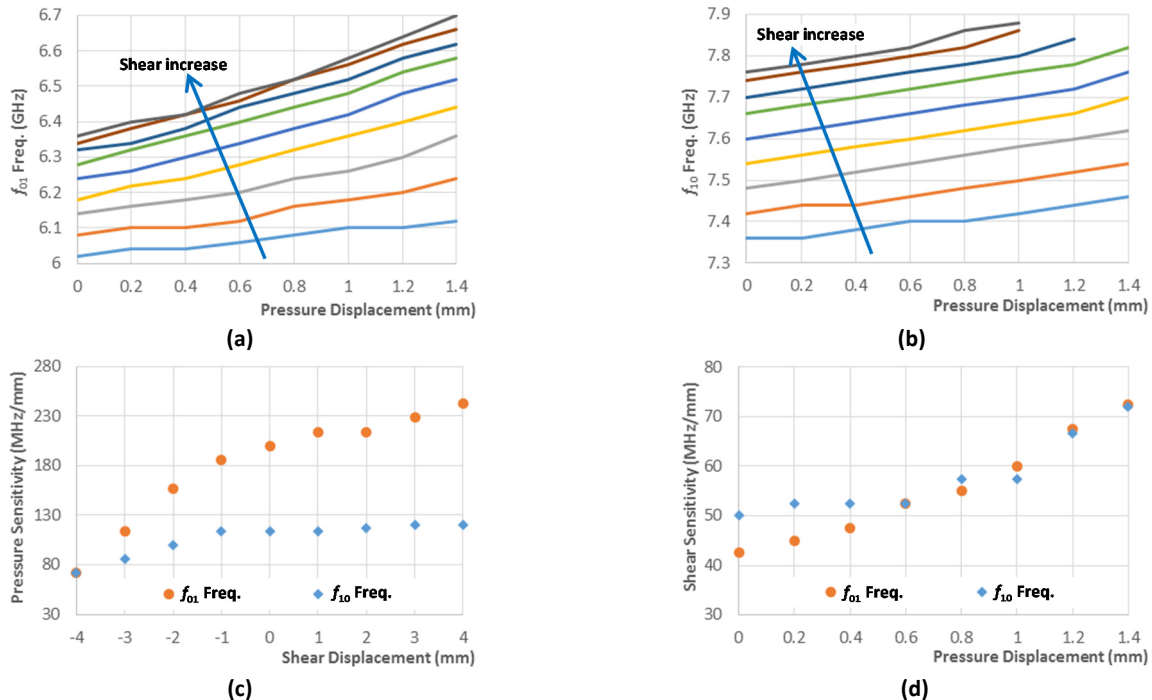

Fig. 5. Simulated results - effects of the shear and pressure displacements on the (a) f_{01} and (b) f_{10} antenna frequencies and their (c) shear and (d) pressure sensitivities.

transmission line. To reduce the computational time, the analysis was carried out using "adaptive sweep". Due to the inset feeding, the impedances of the two antenna resonances are coupled. To find an optimized feeding location, a parameter sweep on (x_0, y_0) was carried out when the director covered one half of the radiation patch along its length direction and was centered along the width direction of the radiation patch (see Fig. 2(a)). The finalized design parameters of the antenna sensor are given in Table I.

The effects of the director position on the antenna resonant frequenceis were studied by assuming the neutral position of the director, *i.e.* with zero pressure and shear displacements, is when the director is 5 mm above the radiation patch and its lower edge is aligned with the center line of the radiation patch. The superstrate height was varied from 5 mm to 3.6 mm at an interval of 0.2 mm, resulting in a total pressure displacement of 1.4 mm. At each pressure displacement, the director was shifted along the shear direction from $s = -4$ mm to 4 mm at an increment of 1 mm, where $s = -4$ mm corresponds to when the lower edge of the director is 4 mm above the center of the radiation patch. The effects of the shear and pressure displacements on the antenna resonant frequencies are shown in Fig. 5. Both frequencies increased with the increase of the pressure displacement, *i.e.* as the director was moved closer to the radiation patch. Similarly, under a constant pressure displacement, the antenna frequencies increased as the director was moved toward the microstrip transmission line. At large shear displacements, *i.e.* when the director was very close to the feeding location, both frequencies become less sensitive to the shear displacement, as shown in Fig. 5(a) and 5(b). In addition, the TM_{10} resonance weakened significantly and it was difficult to detect the f_{10} frequency when both the shear displacement and the pressure displacement are large, resulting in missing data points for pressure displacements larger than 1.0 mm (see Fig. 5(b)). The average shear and pressure sensitivties were calculated at different pressure and shear displacements, respectively. As shown in Fig. 5(c), the shear sensevities are similar for the two antenna resonant frequencies, ranging from around 40 MHz/mm at zero pressure to slightly above 70MHz/mm when the pressure displacement was 1.4 mm. The pressure sensitivies of the antenna resonant frequencies are about two to three times larger than the shear sensitivities. For
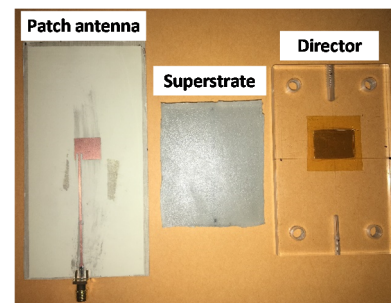

Fig. 6. Components for the antenna shear/pressure displacement sensor.

both frequencies, the pressure sensitivities increased linearly with the shear displacement increase when the shear displacement was negative. These sensitivity increases, however, leveled off when the shear displacement became positive. In addition, the f_{01} frequency displayed a much higher pressure sensitivity than the f_{10} frequency did.

IV. SENSOR FABRICATION AND CHARACTERIZATION

The dual-frequency microstrip patch antenna was fabricated following the same fabrication procedure described above while the director was cut from a thin flexible laminate (Rogers RO3003, 0.125 mm thick). The three components of the antenna shear and pressure displacement sensor, *i.e.* the rectangular patch antenna, the superstrate, and the director are shown in Fig. 6. The patch antenna and the director were taped on base plates using Kapton tape so that they can be installed on a test apparatus that can apply controlled shear and pressure displacements automatically (see section V for details). The superstrate was cut from a commercial prosthetic liner and glued on the patch antenna using an instant-bonding ethyl adhesive (Loctite 4011). The antenna resonant frequencies before and after the application of the adhesive were almost identical, indicating that the adhesive has little effect on the antenna resonant frequencies. The measured S11 curves of the antenna sensor without the superstrate, with the superstrate, and with the director placed at the neutral position are compared with their simulation counterparts in Fig. 7. Again, due to the fabrication variability, the measured frequencies of the antenna sensor without the superstrate were slightly smaller than the simulated values. As predicted by the simulation model, the
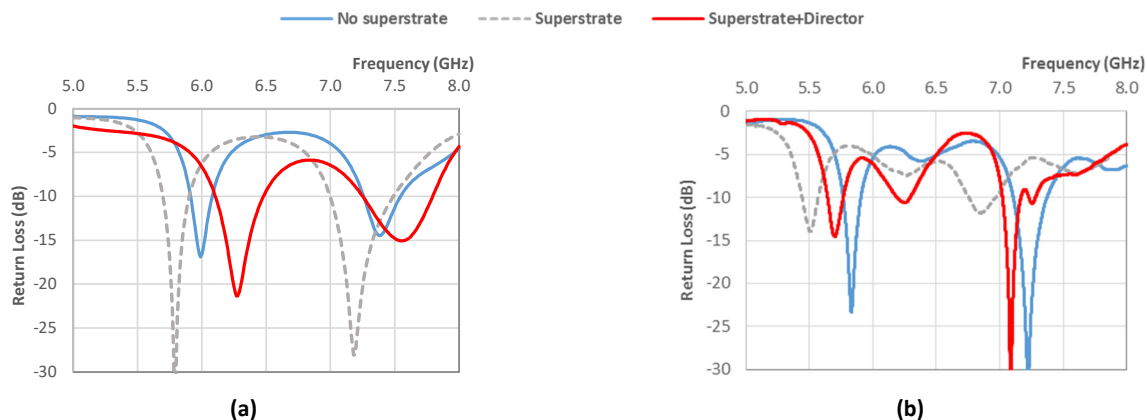

Fig. 7. Effects of the superstrate and director on the resonant frequencies of the dual-frequency patch antenna; (a) simulation and (b) measurement.

measured antenna frequencies shift to lower frequencies when the superstrate was placed on top of the radiation patch, although the actual frequency shifts were slightly larger than the predictions. Similarly, adding the director shifted the antenna frequencies higher. However, the frequency increases due to the director were much smaller than those predicted by the simulation. While the measurement results matched with the simulation model qualitatively, it is, in general, difficult to achieve an exact match between the simulation and measurement due to the sensitivity of the antenna sensor to minute fabrication variations and the difficulty in modeling the nuances of the experiments. For example, the simulation model has a perfect 50 Ω port while soldering may change the impedance of the SMA connector in the experiment. Moreover, the superstrate covers the entire design space, including the port, in the simulation model. In contrast, the superstrate only covers a portion of the microstrip transmission line in the experiment. Other factors, such as the thickness of the superstrate, which was difficult to measure precisely using a caliper due to the softness of the material, and the alignment of the director may also contribute to the observed discrepancies. Therefore, the simulation is only used for the initial design of the antenna sensor but the performance of the antenna sensor was characterized and validated experimentally.

V. Shear and Pressure Testing of Antenna Sensor

A test apparatus that enables applying controlled shear and pressure displacements to the antenna sensor package was implemented and is shown in Fig. 8. The base plate containing the director was installed on the top plate, which is fixed along the vertical direction but can freely slide along the horizontal direction. The base plate containing the patch antenna and the superstrate was installed on the bottom plate that is mounted above a bubble actuator and can freely slide along the vertical direction. Inflating the bubble actuator pushes the bottom plate upward, generating a pressure force on the sensor package. The displacement of the bottom plate was measured using a linear variable differential transformer (LVDT) distance sensor. To apply shear displacements, a rod was screwed on the top plate so that its position can be adjusted using a linear motor. The shear displacement of the top plate was also measured using an LVDT distance sensor, mounted on the opposite side of the shear rod. The resonant frequencies of the microstrip patch antenna were measured by connecting it to a vector network analyzer (VNA) (Rohde & Schwarz, ZVA24) using a coaxial
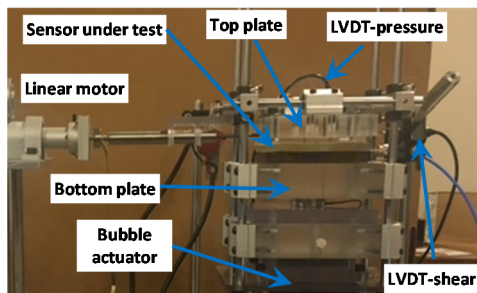

Fig. 8. Mechanical test apparatus for applying controlled shear and pressure displacements on the antenna sensor under test.

cable. The VNA was set to sweep the interrogation frequency from 5 GHz to 8 GHz with 5001 frequency points, resulting in a frequency resolution of 0.6 MHz. An Arduino-based controller was implemented to control the applied shear and pressure displacements and to acquire the shear and pressure displacements from the LVDT sensors. A visual-basic program was developed in Microsoft Excel to communicate with the controller and to acquire the S11 parameters from the VNA automatically. The shear and pressure test was first carried out without gluing the director to the superstrate so that the shear displacement range can be evaluated. Based on this initial test, the neutral position of the director was determined. Subsequently, the director was glued to the superstrate using the same adhesive that glued the superstrate to the radiation patch. After the adhesive was cured, the director was moved away from the neutral position so that the antenna sensor can be tested under different combinations of shear and pressure displacements.

VI. Results and Discussions

The shifts of the antenna resonant frequencies with the applied shear and pressure displacements are plotted in Fig. 9(a) and 9(b). The total pressure displacement applied was 0.78 mm, corresponding to pressurizing the bubble actuator from 0 kpa to 273 kPa at an interval of 19.5 kPa. The total shear displacement was 5.94 mm, $i.e.$ the director was moved from -4.08 mm to 1.86 mm at 13 increments. Both antenna frequencies reduced initially when the pressure displacement was increased from 0 mm to 0.15 mm. Subsequently, the antenna frequencies increased linearly with the increase of the pressure displacement. The inconsistency of the antenna frequency shifts at the low pressure displacements, which is not predicted by the simulation, may be contributed by a thin layer of fabric laminated on the outer surface of the commercial prosthetic liner. Considering that the thin fabric is relatively porous, its thickness and dielectric constant may experience large changes at the initial application of pressure. These parameters, however, will stabilize once the pressure reaches a threshold, beyond which the antenna frequencies are mainly influenced by the compression of the silicone rubber. Another contributor may be the alignment of the bottom plate, which cannot be perfectly leveled initially. We observed that the bottom plate tended to self-level under slight pressure. Since the antenna sensor is unlikely to operate at near zero pressure condition, the measurements obtained below 0.15 mm pressure displacements were excluded, resulting in a pressure operation range of 0.15mm to 0.78 mm. Under a specific pressure displacement, the antenna frequencies increased with the shear displacement increase. At the maximum shear displacement of 1.86 mm, however, the f_{10} frequency was not detected due to the deterioration of the S11 curve. In addition, the measurements at the first shear displacement, $i.e.$ -4.1 mm, were also discarded due to the observation that the start-up of the linear motor may produce unpredictable results. As a result, the shear operation range of the antenna sensor is defined as from -3.6 mm to 1.35mm. The shear and pressure sensitivities of the antenna resonant frequencies for the selected operation range are shown in Fig. 9(c) and 9(d). The shear sensitivity of the f_{01} frequency varies almost linearly from 13 MHz/mm to 19 MHz/mm as the
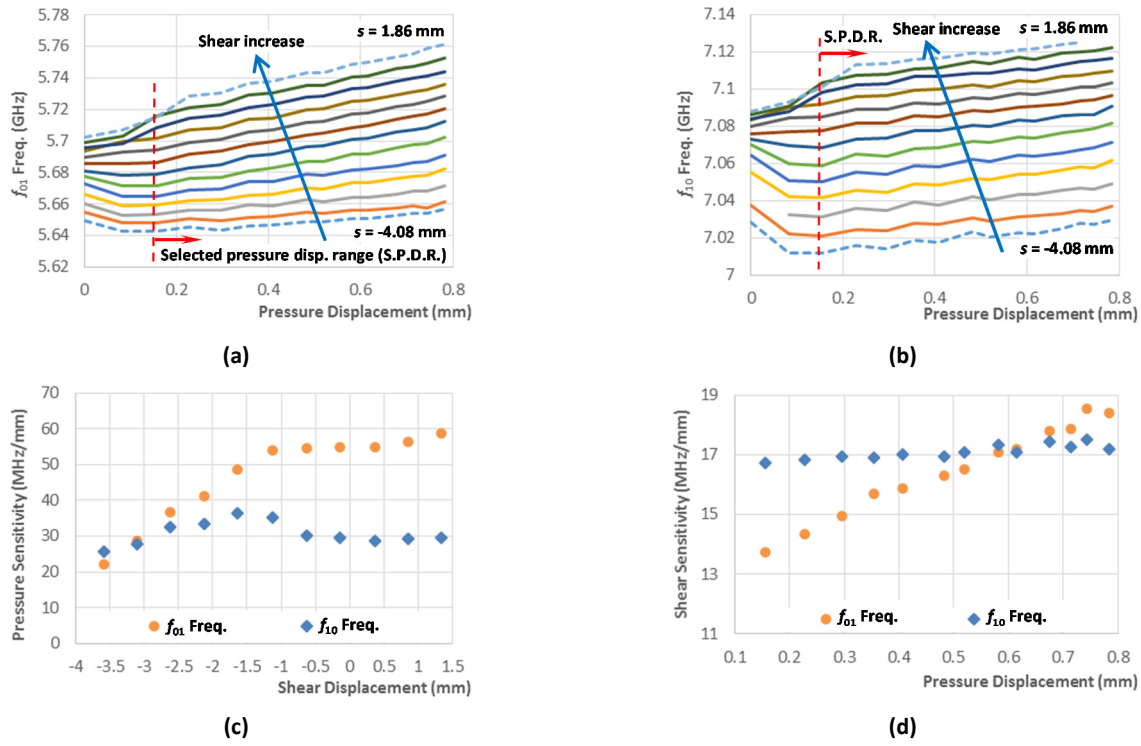
Fig. 9. Measurement results - effects of shear and pressure displacements on the (a) f_{01} and (b) f_{10} antenna frequencies and their (c) shear and (d) pressure sensitivities for the selected operation range of pressure displacements from 0.15 mm to 0.78 mm and shear displacements from -3.6 mm to 1.35 mm. In (a) and (b), only the solid curves, *i.e.* the curves obtained within the shear displacement operation range, were selected for the inverse algorithm.

pressure displacement increases while the shear sensitivity of the f_{01} frequency remains almost constant at around 17MHz/mm. The pressure sensitivities of both frequencies increase steadily when the shear displacement was increased from -3.6 mm to -1.6 mm. The shear sensitivities, however, leveled off when the shear displacement was increased beyond -1.1 mm. Qualitatively, the trends of the measured antenna frequency shifts as well as the shear and pressure sensitivities matched with the simulation predictions. However, the measured sensitivities were three or four times smaller than the simulated values. Again, these discrepancies are likely due to the fact that the simulation model cannot faithfully capture the details of the experiment setup. For example, the simulation model only accounted for the position changes of the director but did not consider the dielectric constant change of the silicone rubber under shear or pressure deformations. Characterizing this factor and incorporating it in the simulation model would require substantial experimental and modeling work, which could be the subject of a separate paper.

In order to inversely determine the shear and pressure displacements from the measured antenna resonant frequencies, a MATLAB program was developed to curve fit the measurement data using bi-variable quadratic functions, *i.e.* $f_{ij} = P_{00} + P_{10} \cdot s + P_{01} \cdot p + P_{11} \cdot s \cdot p + P_{20} \cdot s^2 + P_{02} \cdot p^2$, where s is the shear displacement, p is the pressure displacement, and f_{ij} stands for either f_{01} or f_{10}. R^2 values of 0.9978 and 0.9990 were achieved for the f_{01} and f_{10} frequencies, respectively. The fitting parameters for these two resonance frequencies are given in Table II. The 3D views of the fitting surfaces as well as the measured data are shown in Fig. 10(a) and 10(b). Based on these fitting equations, an algorithm was

developed to extract the shear and pressure displacements from the measured antenna resonance frequencies. The inverse algorithm searches the entire shear operation range s with an increment of 0.01 mm. For each assumed s value, the pressure displacement p is solved from the f_{01} fitting equation, which is a single-variable quadratic function once s and f_{01} are known. The resulting (s, p) pairs are subsequently plugged into the f_{10} fitting equation to calculate the estimated f_{10} frequency. The difference between the estimated and measured f_{10} frequencies was then recorded. After the entire shear displacement range was searched, the (s, p) value that gives the lowest difference between the estimated and measured f_{10} frequencies was selected as the measured shear and pressure displacements. The measured shear and pressure displacements, *i.e.* the values inversely determined from the antenna resonant frequencies, are compared with their actual inputs in Fig. 10(c) and 10(d). Except a few outliers, the errors between the measured displacements and the actual inputs are typically within ± 0.3mm for the shear displacements and within ± 0.15 mm for

TABLE II
FITTING PARAMETERS FOR THE ANTENNA RESONANT FREQUENCIES

Symbol	f_{01} Frequency	f_{10} Frequency
P_{00}	5.64	7.013
P_{10}	0.0142	0.02411
P_{01}	0.01688	0.02623
P_{20}	5.375-6	-0.001217
P_{11}	0.00594	-0.00109
P_{02}	0.01586	0.007403

$f_{ij} = P_{00} + P_{10} \cdot s + P_{01} \cdot p + P_{11} \cdot s \cdot p + P_{20} \cdot s^2 + P_{02} \cdot p^2$ where s is the shear displacement and p is the pressure displacement.
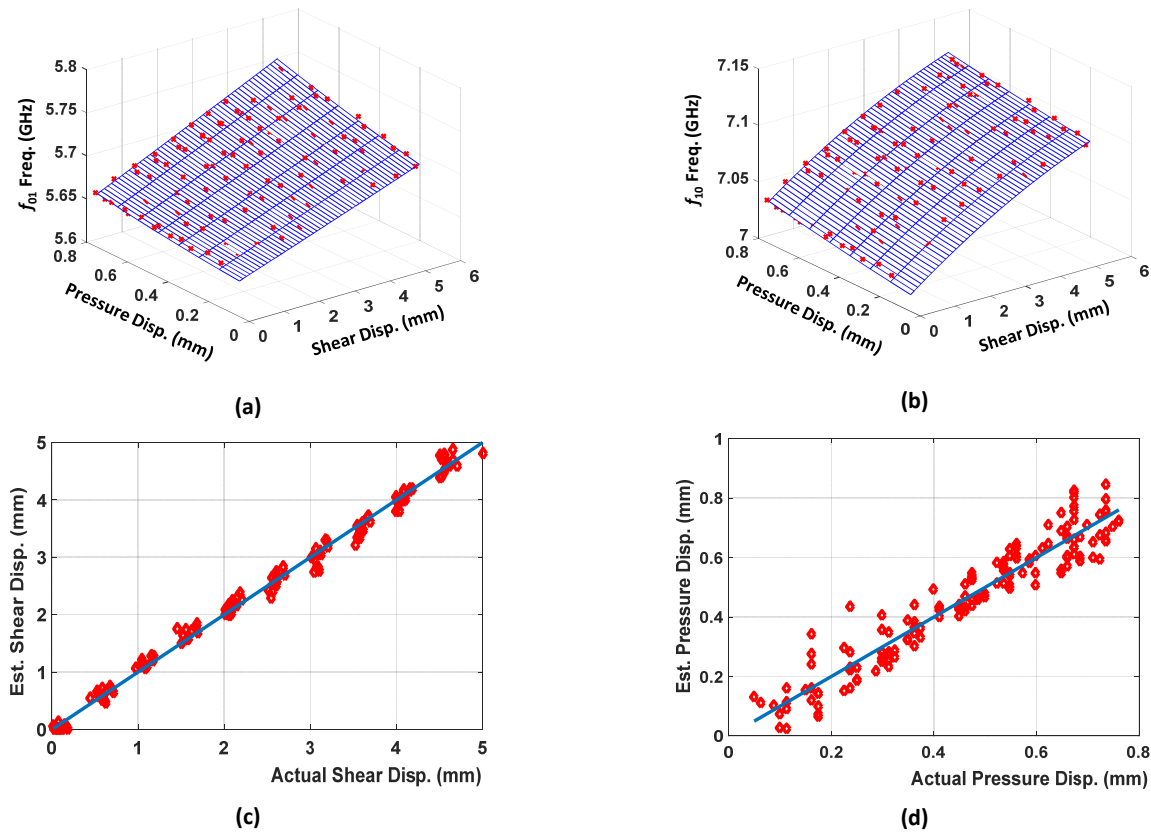
Fig. 10. Deduce the shear and pressure displacements from the measured antenna resonant frequencies; (a) and (b) curve fitting the measured f_{01} and f_{10} frequencies as a bi-variable quadratic function; (c) and (d) comparisons between the shear and pressure displacements inversely determined from the measured f_{01} and f_{10} frequencies with the actual inputs. The blue line represents a perfect match between the estimated and actual values.

the pressure displacements, corresponding to $\pm 5\%$ of the full shear displacement range and $\pm 25\%$ of the full pressure displacement range, respectively. Some of the measurement errors may be contributed by the LVDT sensors, which have measurement uncertainties of 0.06 mm. The measurement errors for the shear displacements are comparable to those of the published sensors [6] while the measurement errors for the pressure displacements, in terms of the percentage of the full range, is slightly higher than that of the pressure sensor commercialized by Tekscan [40], which is widely used in clinical applications. It is worth noting that we were not able to apply pressures beyond 273 kPa to the bubble actuator due to the equipment limitation. Therefore, the full pressure displacement range of the antenna sensor may be larger than what we have obtained in this study. Reducing the height of the superstrate in the future may improve the range and measurement uncertainties of the antenna sensor, especially for the pressure measurements. In addition, we also noticed that the test apparatus introduced slight coupling between the shear and pressure displacements due to the bubble actuator. Replacing the bubble actuator with a linear motor may improve the measurement uncertainties as well. In this study, the antenna sensor was characterized with respect to the shear and pressure displacements. The corresponding shear and pressure forces or stresses can be calculated from the measured displacements once the mechanical properties, namely the shear and compression moduli, of the superstrate material are known. Considering that the shear and pressure stresses for different applications vary widely [6] [40], the mechanical properties of the superstrate material should be characterized and adjusted

for specific applications. For applications that require a finer spatial resolution, the sensor size can be reduced by increasing the antenna resonant frequencies, as indicated by (1). Printed antenna technology could also be adopted to produce distributed antenna sensor arrays on flexible substrates [41].

VII. CONCLUSION

A dual-frequency stacked microstrip patch antenna sensor is presented for simultaneous shear and pressure displacement measurements. By constructing the dual-frequency antenna sensor using a rectangular microstrip patch antenna, a superstrate, and a director, we demonstrated that the shear and pressure displacements between the radiation patch and the director can be inversely determined from the measured antenna resonant frequencies. The typical measurement errors were found to be ±0.3 mm for the shear displacement and within ±0.15 mm for the pressure displacement. Multiplexing the antenna sensors to form distributed sensor arrays will be investigated in the future. A battery-powered portable interrogator is currently under developed to facilitate real-time monitoring on a continuous basis.

REFERENCES

[1] M. T. Francomano, D. Accoto, and E. Guglielmelli, "Artificial sense of slip - A review," IEEE Sens. J., vol. 13, no. 7, pp. 2489–2498, 2013.
[2] S.-K. Hwang and H.-Y. Hwang, "Study on signal characteristic analysis of multi-axis load measurement sensors," Smart Mater. Struct., vol. 25, no. 11, p. 115004, 2016.

[3] A. D. Amore, G. De Maria, L. Grassia, C. Natale, and S. Pirozzi, "Silicone-rubber-based tactile sensors for the measurement of normal and tangential components of the contact force," J. Appl. Polym. Sci., vol. 122, no. 2011, pp. 3758–3770, 2013.

[4] M. Y. Cheng, C. L. Lin, Y. T. Lai, and Y. J. Yang, "A polymer-based capacitive sensing array for normal and shear force measurement," Sensors (Switzerland), vol. 10, no. 11, pp. 10211–10225, 2010.

[5] J. Missinne, E. Bosman, B. Van Hoe, R. Verplancke, G. Van Steenberge, S. Kalathimekkad, P. Van Daele, and J. Vanfleteren, "Two axis optoelectronic tactile shear stress sensor," Sensors Actuators, A Phys., vol. 186, pp. 63–68, 2012.

[6] S. Rajala and J. Lekkala, "Plantar shear stress measurements - A review," Clin. Biomech., vol. 29, no. 5, pp. 475–483, 2014.

[7] M. Yavuz, H. Master, A. Garrett, L. a. Lavery, and L. S. Adams, "Peak plantar shear and pressure and foot ulcer locations: a call to revisit ulceration pathomechanics," Diabetes Care, vol. 38, no. August, p. dc151596, 2015.

[8] J. S. Akins, P. E. Karg, and D. M. Brienza, "Interface shear and pressure characteristics of wheelchair seat cushions," J. Rehabil. Res. Dev., vol. 48, no. 3, pp. 225–234, 2011.

[9] A. F. T. Mak, M. Zhang, and D. A. Boone, "State-of-the-art research in lower-limb prosthetic biomechanics-socket interface: a review," J. Rehabil. Res. Dev., vol. 38, no. 2, pp. 161–74, 2001.

[10] F. A. Appoldt, L. Bennett, and R. Contini, "Tangential pressure measurements in above-knee suction sockets," Bull. Prosthet. Res., vol. 10, no. 13, pp. 70–86, Jan. 1970.

[11] D. Benfield, E. Lou, and W. a Moussa, "Parametric evaluation of shear sensitivity in piezoresistive interfacial force sensors," J. Micromechanics Microengineering, vol. 21, no. 4, p. 45005, Apr. 2011.

[12] Y. Jung, D. G. Lee, J. Park, H. Ko, and H. Lim, "Piezoresistive tactile sensor discriminating multidirectional forces," Sensors (Switzerland), vol. 15, no. 10, pp. 25463–25473, 2015.

[13] C. H. Yang and G. S. Wu, "A contact-type piezoresistive micro-shear stress sensor for above-knee prosthesis application," J. Microelectromechanical Syst., vol. 10, no. 1, pp. 121–127, Mar. 2001.

[14] P. Laszczak, M. McGrath, J. Tang, J. Gao, L. Jiang, D. L. Bader, D. Moser, and S. Zahedi, "A pressure and shear sensor system for stress measurement at lower limb residuum/socket interface," Med. Eng. Phys., vol. 0, pp. 1–6, 2016.

[15] C. Murakami, Y. Ishikuro, and M. Takahashi, "Feasibility of novel four degrees of freedom capacitive force sensor for skin interface force.," Biomed. Eng. Online, vol. 11, no. 1, p. 90, 2012.

[16] K. Sundara-Rajan, G. I. Rowe, A. Bestick, A. V. Mamishev, G. K. Klute, and W. R. Ledoux, "Capacitive sensing of interfacial forces in prosthesis," 2010 IEEE Int. Work. Med. Meas. Appl., no. 2, pp. 73–76, Apr. 2010.

[17] L. S. Lincoln, S. J. M. Bamberg, E. Parsons, C. Salisbury, and J. Wheeler, "An elastomeric insole for 3-axis ground reaction force measurement," in Proceedings of the IEEE RAS and EMBS International Conference on Biomedical Robotics and Biomechatronics, 2012, pp. 1512–1517.

[18] L. S. Lincoln, M. Quigley, B. Rohrer, C. Salisbury, and J. Wheeler, "An optical 3D force sensor for biomedical devices," in Proceedings of the IEEE RAS and EMBS International Conference on Biomedical Robotics and Biomechatronics, 2012, pp. 1500–1505.

[19] L. Du, X. Zhu, and J. Zhe, "An inductive sensor for real-time measurement of plantar normal and shear forces distribution," IEEE Trans. Biomed. Eng., vol. 62, no. 5, pp. 1316–1323, 2015.

[20] Z. F. Zhang, X. M. Tao, H. P. Zhang, and B. Zhu, "Soft fiber optic sensors for precision measurement of shear stress and pressure," IEEE Sens. J., vol. 13, no. 5, pp. 1478–1482, 2013.

[21] W. C. Wang, W. R. Ledoux, B. J. Sangeorzan, and P. G. Reinhall, "A shear and plantar pressure sensor based on fiber-optic bend loss," J. Rehabil. Res. Dev., vol. 42, pp. 315–326, 2005.

[22] A. Candiani, W. Margulis, M. Konstantaki, and S. Pissadakis, "Ferrofluid-infiltrated optical fibers for shear-sensing smart pads," SPIE Newsroom, pp. 11–13, 2012.

[23] G. Marrocco, L. Mattioni, and C. Calabrese, "Multiport Sensor RFIDs for Wireless Passive Sensing of Objects—Basic Theory and Early Results," IEEE Trans. Antennas Propag., vol. 56, no. 8, pp. 2691–2702, Aug. 2008.

[24] S. Caizzone, G. Marrocco, and I. Member, "RFID-Grids for deformation sensing," in 2012 IEEE International Conference on RFID, 2012, pp. 130–134.

[25] C. Mandel, B. Kubina, M. Schüßler, and R. Jakoby, "Passive chipless wireless sensor for two-dimensional displacement measurement," in Proceedings of the 41st European Microwave Conference, 2011, pp. 79–82.

[26] D. J. J. Thomson, D. Card, and G. E. E. Bridges, "RF cavity passive wireless sensors with time-domain gating-based interrogation for SHM of civil structures," IEEE Sensors J., vol. 9, no. 11, p. 1430, 2009.

[27] T. T. Thai, H. Aubert, P. Pons, G. Dejean, M. M. Tentzeris, and R. Plana, "Novel design of a highly sensitive RF strain transducer for passive and remote sensing in two dimensions," IEEE Trans. Microw. Theory Tech., vol. 61, no. 3, pp. 1385–1396, 2013.

[28] H. Aubert, F. Chebila, M. Jatlaoui, T. Thai, H. Hallil, A. Traille, S. Bouaziz, A. Rifaï, P. Pons, P. Menini, and M. Tentzeris, "Wireless sensing and identification of passive electromagnetic sensors based on millimetre-wave FMCW RADAR," in IEEE 2012 International Conference on RFID-Technologies and Applications (RFID-TA), 2012, pp. 398–403.

[29] H. Huang, "Antenna Sensors in Passive Wireless Sensing Systems," in Handbbok of Antenna Technologies, Z. N. Chen, Ed. Singapore: Springer Reference, 2015, pp. 1–34.

[30] H. Huang, "Flexible wireless antenna sensor: a review," IEEE Sens. J., vol. 13, no. 10, pp. 3865–3872, 2013.

[31] I. Mohammad and H. Huang, "Shear sensing based on a microstrip patch antenna," Meas. Sci. Technol., vol. 23, no. 10, p. 105705, Oct. 2012.

[32] I. Mohammad and H. Huang, "Pressure and shear sensing based on microstrip antennas," in Proceedings of SPIE Vol. 8345, 2012, vol. 8345, p. 83451D–83451D–8.

[33] X. Xu and H. Huang, "Battery-less wireless interrogation of microstrip patch antenna for strain sensing," Smart Mater. Struct., vol. 21, no. 12, p. 125007, Dec. 2012.

[34] X. Yi, T. Wu, Y. Wang, R. T. Leon, M. M. Tentzeris, and G. Lantz, "Passive wireless smart-skin sensor using RFID-based folded patch antennas," Int. J. Smart Nano Mater., vol. 2, no. 1, pp. 22–38, Feb. 2011.

[35] C. A. Balanis, Antenna Theory: Analysis and Design, 3rd Editio. Hoboken, New Jersey: John Wiley & Sons, Inc, 2005.

[36] I. J. Bahl, P. Bhartia, and S. S. Stuchly, "Design of microstrip antennas covered with a dielectric layer," IEEE Trans. Antennas Propag., vol. AP-30, no. 2, pp. 314–318, 1982.

[37] M. Rodrigues and C. M. Furse, "An implantable antenna designed for ease of manufacturing," Microw. Opt. Technol. Lett., vol. 54, no. 12, pp. 2781–2784, 2012.

[38] B. Kaur, G. Saini, and A. Saini, "Silicone rubber superstrate loaded patch antenna design using slotting technique," IOP Conf. Ser. Mater. Sci. Eng., vol. 149, p. 12150, 2016.

[39] U. Tata, H. Huang, R. L. Carter, and J. C. Chiao, "Exploiting a patch antenna for strain measurements," Meas. Sci. Technol., vol. 20, no. 1, p. 15201, Jan. 2009.

[40] A. H. Abdul Razak, A. Zayegh, R. K. Begg, and Y. Wahab, "Foot plantar pressure measurement system: a review," Sensors (Switzerland), vol. 12, no. 7, pp. 9884–9912, 2012.

[41] C. Reig and E. Avila-Navarro, "Printed antennas for sensor applications: a review," IEEE Sens. J., vol. 14, no. 8, pp. 2406–2418, 2014.

Haiying Huang (M'98) received the Bachelor of Engineering degree in Aircraft Propulsion from the Beijing University of Aeronautics and Astronautics (BUAA) in 1987. She received the M.S. degree in Electrical Engineering in 1997 and the Ph.D. degree in Aerospace Engineering in 1998; both from the Georgia Institute of Technology. Her current research interests include developing sensors for health monitoring of manmade and biological mechanical systems. She is the head of the Advanced Sensors Technology Laboratory (ASTL) at the University of Texas Arlington (UTA).

Farnaz Farahanipad received her Bachelor of Engineering degree in Electrical Engineering from the Garmsar Azad Univeriusity, Garmsar, Iran in 2007 and her M.S. in Electrical Engineering from Arak Azad University, Arak, Iran in 2012. In 2016, she started her second M.S. study in Computer Science at UTA and later joined the ASTL as a graduate research assistant. Her research interests cover wireless sensors, circuit design, telecommunication, digital signal processing and data mining.

Abhay Kumar Singh received his bachelor's degree in Mechanical Engineering from Panjab University, Chandigarh, in 2013. Thereafter, he joined the design and research team of Oceaneering, an oil and gas industry. In 2014, he decided to pursue further education by joining UTA as a graduate research assistant. He earned his MSc. degree, in mechanical engineering, in Dec 2016.